

Multi-messenger constraints on dark matter annihilation into electron-positron pairs

M. Wechakama^{1*} and Y. Ascasibar²

¹*Leibniz-Institut für Astrophysik Potsdam, An der Sternwarte 16, Potsdam 14482, Germany*

²*Departamento de Física Teórica, Universidad Autónoma de Madrid, Madrid 28049, Spain*

Draft version 1.0 (12 December 2012)

ABSTRACT

We investigate the production of electrons and positrons in the Milky Way within the context of dark matter annihilation. Upper limits on the relevant cross-section are obtained by combining observational data at different wavelengths (from Haslam, WMAP, and Fermi all-sky intensity maps) with recent measurements of the electron and positron spectra in the solar neighbourhood by PAMELA, Fermi, and HESS. We consider synchrotron emission in the radio and microwave bands, as well as inverse Compton scattering and final-state radiation at gamma-ray energies. For most values of the model parameters, the tightest constraints are imposed by the local *positron* spectrum and the final-state radiation from the central regions of the Galaxy. According to our results, the dark matter annihilation cross-section into electron-positron pairs should not be higher than the canonical value for a thermal relic if the mass of the dark matter candidate is smaller than a few GeV. In addition, we also derive a stringent upper limit on the inner logarithmic slope α of the density profile of the Milky Way dark matter halo ($\alpha < 1.3$ if $m_{\text{dm}} < 100$ GeV and $\alpha < 1.8$ if $m_{\text{dm}} < 10$ TeV) assuming that $\langle\sigma v\rangle_{e^\pm} = 3 \times 10^{-26} \text{ cm}^3 \text{ s}^{-1}$.

Key words: dark matter – astroparticle physics – radiation mechanisms: non-thermal – Galaxy: structure

1 INTRODUCTION

Dark matter can be indirectly detected through the signatures of standard model particles produced by its annihilation or decay (see e.g. Bertone et al. 2005; Bertone 2010). A great deal of work has focused on the emission of gamma rays from the Galactic centre (e.g. Berezhinsky et al. 1994; Bergström et al. 1998; Baltz & Edsjö 1999; Gondolo & Silk 1999; Morselli et al. 2002; Ullio et al. 2002; Stoehr et al. 2003; Peirani et al. 2004; Prada et al. 2004; Cesarini et al. 2004; Bergström et al. 2005a,b; Profumo 2005; Aharonian et al. 2006; Zaharijas & Hooper 2006; Boyarsky et al. 2008; Pospelov et al. 2008; Springel et al. 2008; Bell & Jacques 2009; Cirelli & Panci 2009; Fornasa et al. 2009; Bernal & Palomares-Ruiz 2010; Abazajian et al. 2010; Cirelli et al. 2010; Papucci & Strumia 2010; Hooper & Goodenough 2011; Hooper & Linden 2011a,b; Ackermann et al. 2012, among many others), the Milky Way satellites (e.g. Baltz et al. 2000; Tyler 2002; Baltz & Wai 2004; Hooper et al. 2004; Bergström & Hooper 2006; Sánchez-Conde et al. 2007; Strigari et al. 2007, 2008; Wood et al. 2008; Martinez et al.

2009; Abdo et al. 2010; Acciari et al. 2010; Essig et al. 2009, 2010; Ackermann et al. 2011; Abramowski et al. 2011), and galaxy clusters (e.g. Colafrancesco et al. 2006; Jeltema et al. 2009; Ackermann et al. 2010a; Sánchez-Conde et al. 2011; Pinzke et al. 2011). Prospects for indirect dark matter detection in the microwave background have also been considered by several authors (e.g. Blasi et al. 2003; Colafrancesco 2004; Padmanabhan & Finkbeiner 2005; Mapelli et al. 2006; Zhang et al. 2006, 2007; Cholis et al. 2009; Galli et al. 2009; Slatyer et al. 2009; Kanzaki et al. 2010; Lavalle 2010; Hütsi et al. 2011; Galli et al. 2011; McQuinn & Zaldarriaga 2011; Delahaye et al. 2012), as well as X-ray (e.g. Abazajian et al. 2001; Boyarsky et al. 2007, 2008; Zavala et al. 2011), radio (e.g. Colafrancesco & Mele 2001; Aloisio et al. 2004; Bergström et al. 2009; Borriello et al. 2009; Ishiwata et al. 2009; Fornengo et al. 2012) and multi-wavelength signatures (e.g. Regis 2008; Regis & Ullio 2008; Bertone et al. 2009; Pato et al. 2009; Profumo & Ullio 2010; Crocker et al. 2010).

The recent results from indirect detection experiments in the solar neighbourhood have also suggested the possibility that such a signature has been seen. In particular, the PAMELA experiment has pointed a significant excess

* E-mail: maneenate@aip.de(MW); yago.ascasibar@uam.es (YA)

of electrons and positrons above the expected smooth astrophysical background (Adriani et al. 2009a). If these results are interpreted in terms of dark matter annihilation, then an abundant population of high-energy e^\pm is being created everywhere in the Galactic dark matter halo, with the associated final-state radiation (FSR), as well as synchrotron emission in the Galactic magnetic field and inverse Compton scattering (ICS) of the photons of the interstellar radiation field (ISRF).

Although the currently most favoured explanation for the origin of Galactic positrons, traced by the positron annihilation emission line at 511 keV (see Prantzos et al. 2011, for a recent review) is low-mass X-ray binaries (Weidenspointner et al. 2008), and the local positron excess at high energies is most likely due to the contribution of nearby pulsars (see e.g. Profumo 2012), several works have considered the possibility that dark matter annihilation makes a sizeable contribution to the positron budget of the Milky Way (e.g. Boehm et al. 2004; Boehm & Ascasibar 2004; Beacom et al. 2005; Picciotto & Pospelov 2005; Ascasibar et al. 2006; Beacom & Yüksel 2006; Sizun et al. 2006; Finkbeiner & Weiner 2007; Pospelov & Ritz 2007; Barger et al. 2009; Bergström et al. 2009; Chen & Takahashi 2009; Cholis et al. 2009; Cirelli et al. 2009; Donato et al. 2009; Grasso et al. 2009; Malyshev et al. 2009; Mertsch & Sarkar 2009; Regis & Ullio 2009; Yin et al. 2009; Chen et al. 2010; Meade et al. 2010; Cline et al. 2011; Vincent et al. 2012).

The present work focuses on the astrophysical signatures of dark matter annihilation into electron-positron pairs, neglecting other processes, such as dark matter decay, or other annihilation products, such as protons and antiprotons (whose contribution is severely constrained by recent observational data; see e.g. Adriani et al. 2009b). We try to impose robust, yet stringent constraints on the relevant cross-section by comparing the predictions of an analytic model of particle propagation with a multi-wavelength set of observational data obtained from the literature. More precisely, we compare the expected emission from synchrotron radiation, ICS and FSR within the Milky Way with 18 maps of the sky at different frequencies: the Haslam radio map at 408 MHz, the 7-year data from the Wilkinson Microwave Anisotropy Probe (WMAP) in its 5 bands (23 GHz, 33 GHz, 41 GHz, 61 GHz, and 94 GHz), and gamma-ray maps from the Fermi Large Area Telescope (LAT) binned in 12 different channels (from 0.3 to 300 GeV). A straightforward statistical criterion is used in order to mask the most obvious astrophysical signals (i.e. emission from the galactic disc and point sources), and observational upper limits are derived from the remaining spherically-symmetric component.

In addition to the photon data, we also consider the recent measurements of the local electron and positron spectra performed by PAMELA (Adriani et al. 2009a, 2010, 2011), Fermi (Ackermann et al. 2010b, 2012), and HESS (Aharonian et al. 2008). As will be shown below, considering the positron spectrum separately (rather than the combined electron+positron spectrum) yields a significant improvement on the maximum value allowed for the positron injection rate or, equivalently, the dark matter annihilation cross-section.

Rather than focusing on a particular dark matter candidate, we adopt a model-independent approach (see e.g.

Wechakama & Ascasibar 2011), in which all the injected particles are created with the same initial energy E_0 , of the order of the mass of the dark matter particle. Since this mass is usually much larger than the rest mass of the electron, electrons and positrons will be relativistic at the moment of their creation. However, they can efficiently lose their energy through different processes, such as ICS, synchrotron radiation, Coulomb collisions, bremsstrahlung, and ionization. Throughout this paper, we will often use the Lorentz factor γ to express the energy $E = \gamma m_e c^2$ of the annihilation products, where m_e denotes the rest mass of electron, and c is the speed of light. We will first discuss the results obtained for a ‘canonical’ model of the Milky Way model and then explore the effects of varying the intensity of magnetic field, the diffusion coefficient, the ISRF, and the inner logarithmic slope of dark matter density profile.

The remainder of this paper is structured as follows: Section 2 describes the procedure followed to estimate the electron-positron spectrum, the surface brightness profiles, and the parameters of the Milky Way model. Our analysis of the observational data is fully described in Section 3 (tables with precise numeric values are provided as an appendix), and Section 4 is devoted to the constraints on the dark matter annihilation cross-section. The effect of the different astrophysical parameters is discussed in Section 5, while Section 6 focuses on the constraints that one can impose on the slope of the dark matter density profile by assuming that dark matter particles are produced as thermal relics in the primordial universe. Finally, our main conclusions are succinctly summarized in Section 7.

2 MODEL PREDICTIONS

2.1 Electron-positron propagation

As in our previous work (Wechakama & Ascasibar 2011), the propagation of electrons and positrons through the interstellar medium (ISM) is determined by the diffusion-loss equation

$$\begin{aligned} \frac{\partial}{\partial t} \frac{dn}{d\gamma}(\mathbf{x}, \gamma) &= \nabla \left[K(\mathbf{x}, \gamma) \nabla \frac{dn}{d\gamma}(\mathbf{x}, \gamma) \right] \\ &+ \frac{\partial}{\partial \gamma} \left[b(\mathbf{x}, \gamma) \frac{dn}{d\gamma}(\mathbf{x}, \gamma) \right] \\ &+ Q(\mathbf{x}, \gamma). \end{aligned} \quad (1)$$

We assume a diffusion coefficient of the form

$$K(\gamma) = K_0 \gamma^\delta \quad (2)$$

independent of Galactic location. The values of K_0 and δ corresponding to the three models discussed by Donato et al. (2004) are provided in Table 1 below. The energy loss rate

$$b(\mathbf{x}, \gamma) \equiv -\frac{d\gamma}{dt}(\mathbf{x}, \gamma) = \sum_i b_i(\mathbf{x}, \gamma) \quad (3)$$

is a sum over the relevant physical processes, and the source term $Q(\mathbf{x}, \gamma)$ represents the instantaneous electron-positron injection rate.

Given enough time (of the order of 100 Myr; c.f. Figure 2 in Wechakama & Ascasibar 2011), the electron-

positron population will approach a steady-state distribution, $\frac{\partial}{\partial t} \frac{dn}{d\gamma}(\mathbf{x}, \gamma) = 0$. Assuming that $b(\mathbf{x}, \gamma)$ varies smoothly in space, the particle spectrum fulfills the relation

$$\frac{\partial y(\mathbf{x}, \gamma)}{\partial \gamma} + \frac{K(\gamma)}{b(\gamma)} \nabla^2 y(\mathbf{x}, \gamma) = -Q(\mathbf{x}, \gamma), \quad (4)$$

where

$$y(\mathbf{x}, \gamma) \equiv b(\gamma) \frac{dn}{d\gamma}(\mathbf{x}, \gamma). \quad (5)$$

Imposing $\frac{dn}{d\gamma}(\mathbf{x}, \gamma) = 0$ at infinity, one obtains the Green's function

$$G(\mathbf{x}, \gamma, \mathbf{x}_s, \gamma_s) = \frac{\exp\left(-\frac{|\mathbf{x}-\mathbf{x}_s|^2}{2\Delta\lambda^2}\right)}{(2\pi\Delta\lambda^2)^{3/2}} \Theta(\gamma - \gamma_s) \quad (6)$$

and either the image charges method or an expansion over the eigenfunctions of the linear differential operator may be used to derive the Green's function for other boundary conditions (see e.g. Baltz & Edsjö 1999; Delahaye et al. 2009). The electron-positron spectrum is thus given by

$$\frac{dn}{d\gamma}(\mathbf{x}, \gamma) = \frac{1}{b(\mathbf{x}, \gamma)} \int_{\gamma}^{\infty} d\gamma_s \int_0^{\infty} d^3\mathbf{x}_s \frac{\exp\left(-\frac{|\mathbf{x}-\mathbf{x}_s|^2}{2\Delta\lambda^2}\right)}{(2\pi\Delta\lambda^2)^{3/2}} Q(\mathbf{x}_s, \gamma_s), \quad (7)$$

where the quantity

$$\Delta\lambda^2 = \lambda^2(\gamma) - \lambda^2(\gamma_s) \quad (8)$$

is related to the characteristic diffusion length of the electrons and positrons, γ_s denotes their initial energy, and the variable λ is defined as

$$\lambda^2(\gamma) = \int_{\gamma}^{\infty} \frac{2K(\gamma')}{b(\gamma')} d\gamma'. \quad (9)$$

Considering the dark matter halo as a spherically-symmetric source, the spatial integral can be reduced to one dimension, and the electron-positron spectrum is finally given by the expression

$$\begin{aligned} \frac{dn}{d\gamma}(r, \gamma) &= \frac{1}{b(\gamma)} \frac{\exp\left(-\frac{r^2}{2\Delta\lambda^2}\right)}{(2\pi r^2 \Delta\lambda^2)^{1/2}} \\ &\times \left\{ \int_{\gamma}^{\infty} d\gamma_s \int_0^{\infty} dr_s r_s \exp\left(-\frac{r_s^2}{2\Delta\lambda^2}\right) \right. \\ &\times \left[\exp\left(\frac{rr_s}{\Delta\lambda^2}\right) - \exp\left(-\frac{rr_s}{\Delta\lambda^2}\right) \right] Q(r_s, \gamma_s) \Big\}. \quad (10) \end{aligned}$$

2.2 Loss rates

Electrons and positrons can lose their energy by several physical processes as they move through the ISM. We consider ICS of cosmic microwave background (CMB), starlight and infrared photons, synchrotron radiation, Coulomb collisions, bremsstrahlung, and ionization of neutral hydrogen atoms.

The energy loss rates depend on the energy of the particle. High-energy electrons and positrons mainly lose energy by ICS (e.g. Sarazin 1999). The relevant loss function is

$$b_{\text{ICS}}(\gamma) = \frac{4}{3} \frac{\sigma_T}{m_e c} \gamma^2 U_{\text{rad}}, \quad (11)$$

where σ_T is the Thomson cross section. The combined radiation energy density of the CMB, starlight (SL), and

infrared (IR) light from thermal dust emission (see e.g. Porter & Strong 2005; Porter et al. 2008) is represented by three grey bodies,

$$U_{\text{rad}} = \frac{4\sigma_{\text{SB}}}{c} \left(T_{\text{CMB}}^4 + \mathcal{N}_{\text{SL}} T_{\text{SL}}^4 + \mathcal{N}_{\text{IR}} T_{\text{IR}}^4 \right) \quad (12)$$

where T_i and \mathcal{N}_i represent the effective temperature and the normalization of each component, respectively, and σ_{SB} is the Stefan-Boltzmann constant. The cosmic microwave background is modeled as a perfect black body with temperature $T_{\text{CMB}} = 2.726$ K (Fixsen 2009), and we follow Cirelli & Panci (2009) for the two other components (see Table 2 below).

Synchrotron radiation is another important loss mechanism at high energies. The expression for the loss rate is similar to that of ICS, substituting the radiation energy density in equation (11) by the energy density of the magnetic field, $U_B = B^2/(8\pi)$, where B is the intensity of the magnetic field:

$$b_{\text{syn}}(\gamma) = \frac{4}{3} \frac{\sigma_T}{m_e c} \gamma^2 U_B. \quad (13)$$

For lower-energy electrons and positrons, Coulomb interactions with the thermal plasma must be taken into account. The loss rate is approximately (Rephaeli 1979)

$$b_{\text{Coul}}(\gamma) \approx 1.2 \times 10^{-12} n_e \left[1 + \frac{\ln(\gamma/n_e)}{75} \right] s^{-1}, \quad (14)$$

where n_e is the number density of thermal electrons.

Collisions with thermal ions and electrons also produce radiation through bremsstrahlung. The loss rate due to bremsstrahlung can be approximated as (Blumenthal & Gould 1970)

$$b_{\text{brem}}(\gamma) \approx 1.51 \times 10^{-16} n_e \gamma [\ln(\gamma) + 0.36] s^{-1}. \quad (15)$$

Additional energy losses come from the ionization of hydrogen atoms. The loss rate is given in Longair (1981),

$$\begin{aligned} b_{\text{ion}}(\gamma) &= \frac{q_e^4 n_H}{8\pi\epsilon_0^2 m_e^2 c^3 \sqrt{1 - \frac{1}{\gamma^2}}} \times \left[\ln \frac{\gamma(\gamma^2 - 1)}{2 \left(\frac{I}{m_e c^2}\right)^2} \right. \\ &\quad \left. - \left(\frac{2}{\gamma} - \frac{1}{\gamma^2} \right) \ln 2 + \frac{1}{\gamma^2} + \frac{1}{8} \left(1 - \frac{1}{\gamma} \right)^2 \right], \quad (16) \end{aligned}$$

where n_H is the number density of hydrogen atoms, q_e is the electron charge, ϵ_0 is the permittivity of free space, and I is the ionization energy of the hydrogen atom. The number density of thermal electrons and neutral atoms can be expressed in terms of the total ISM gas density ρ_g and the ionization fraction X_{ion} as

$$n_e = \frac{\rho_g}{m_p} X_{\text{ion}} \quad (17)$$

and

$$n_H = \frac{\rho_g}{m_p} (1 - X_{\text{ion}}), \quad (18)$$

respectively.

2.3 Source term

Since the electrons and positrons in our model originate from the annihilation of dark matter particles, the instantaneous production rate at any given point can be expressed as

$$Q(r, \gamma) = \eta n_{\text{dm}}(r) n_{\text{dm}^*}(r) \langle \sigma v \rangle_{e^\pm} \frac{dN_{e^\pm}}{d\gamma}(\gamma), \quad (19)$$

where n_{dm} and n_{dm^*} denote the number densities of dark matter particles and anti-particles, respectively, $\langle \sigma v \rangle_{e^\pm}$ is the thermal average of the annihilation cross-section times the dark matter relative velocity, and $\frac{dN_{e^\pm}}{d\gamma}$ is the injection spectrum of electrons and positrons in the final state. For self-conjugate dark matter particles, $n_{\text{dm}} = n_{\text{dm}^*} = \frac{\rho_{\text{dm}}}{m_{\text{dm}}}$ and $\eta = 1/2$ in order to avoid double counting; else, $n_{\text{dm}} = n_{\text{dm}^*} = \frac{1}{2} \frac{\rho_{\text{dm}}}{m_{\text{dm}}}$ and $\eta = 1$.

We assume that each annihilation event injects one electron and one positron with roughly the same energy $\gamma_0 \sim m_{\text{dm}}/m_e$,

$$\frac{dN_{e^\pm}}{d\gamma}(\gamma) = 2 \delta(\gamma - \gamma_0), \quad (20)$$

where $\delta(\gamma - \gamma_0)$ denotes a Dirac delta function. Although this is a rather coarse approximation, it has the advantage of being model-independent. For self-conjugate dark matter particles, we obtain

$$Q(r, \gamma) = \left[\frac{\rho_{\text{dm}}(r)}{m_{\text{dm}}} \right]^2 \langle \sigma v \rangle_{e^\pm} \delta(\gamma - \gamma_0). \quad (21)$$

We consider a spherically-symmetric halo, described by a density profile of the form

$$\rho_{\text{dm}}(r) = \frac{\rho_s}{\left(\frac{r}{r_s}\right)^\alpha \left(1 + \frac{r}{r_s}\right)^{3-\alpha}}, \quad (22)$$

where r_s and ρ_s denote a characteristic density and radius of the halo, respectively, and α is the inner logarithmic slope of the density profile. Local inhomogeneities that would boost the expected signal, such as small-scale clumpiness or the presence of subhaloes, are not taken into account. The shape of the dark matter density profile in the inner regions is far from being a settled question. N-body simulations suggest that, at least in the absence of baryons, the profile should be quite steep near the centre ($\alpha \sim 1$), in apparent contradiction with observations. Traditionally, it has been argued that the presence of gas and stars makes the profile even steeper due to the effects of adiabatic contraction (Blumenthal et al. 1986), although some recent claims have also been made in the opposite direction (e.g. El-Zant et al. 2001; Mashchenko et al. 2006; Oh et al. 2010). Given the current uncertainties, we have left the inner slope of the density profile as a free parameter of the model.

2.4 Surface brightness profile

Once the electron-positron spectrum is computed, the emission coefficient¹ for photons of frequency ν is given by the integral

$$\epsilon_\nu(r, \nu) = \frac{1}{4\pi} \int_1^\infty \frac{dn}{d\gamma}(r, \gamma) j(\gamma, \nu) d\gamma, \quad (23)$$

of the electron-positron spectrum $\frac{dn}{d\gamma}(r, \gamma)$ times the specific luminosity $j(\gamma, \nu)$ emitted at frequency ν by a single electron or positron with Lorentz factor γ . The intensity from any

given direction in the sky is simply the integral along the line of sight of the emission coefficient. Since we assume a spherically-symmetric source, it will only depend on the angular separation θ with respect to the Galactic centre,

$$I_\nu(\theta, \nu) = \int_0^\infty \epsilon(r, \nu) ds, \quad (24)$$

where s represents the distance along the line of sight, and the radial distance r to the centre of the Milky Way at any point along the ray is

$$r = \sqrt{x^2 + y^2}, \quad (25)$$

with $x = s \sin \theta$, $y = s \cos \theta - R_\odot$, and $R_\odot = 8.5$ kpc (the distance of the Sun from the Galactic centre).

The contribution of synchrotron radiation, which dominates at low photon energies, can be estimated as (see e.g. Sarazin 1999)

$$j_{\text{syn}}(\gamma, \nu) = \frac{\sqrt{3} q_e^3 B}{m_e c^2} R[\chi(\gamma)], \quad (26)$$

where q_e is the electron charge, B is the intensity of the magnetic field, and the function $R(\chi)$ is defined as (e.g. Ghisellini et al. 1988)

$$R(\chi) \equiv 2\chi^2 \left[K_{\frac{4}{3}}(\chi) K_{\frac{1}{3}}(\chi) - \frac{3}{5} \chi \left\{ K_{\frac{4}{3}}^2(\chi) - K_{\frac{1}{3}}^2(\chi) \right\} \right]. \quad (27)$$

In this expression, K refers to the modified Bessel function, and the normalized frequency

$$\chi \equiv \frac{\nu}{3\gamma^2 \nu_c} \quad (28)$$

is expressed in terms of the cyclotron frequency

$$\nu_c \equiv \frac{q_e B}{2\pi m_e c}. \quad (29)$$

At high photon energies (i.e. gamma rays), we consider the contributions of inverse Compton scattering and final-state radiation. For ICS (e.g. Sarazin 1999)

$$j_{\text{ICS}}(\gamma, \nu) = 12\pi\sigma_T \int_0^1 J\left(\frac{\nu}{4\gamma^2\eta}\right) \mathcal{F}(\eta) d\eta, \quad (30)$$

with σ_T denoting the Thomson cross-section and

$$\mathcal{F}(\eta) \equiv 1 + \eta + 2\eta \ln \eta - 2\eta^2. \quad (31)$$

Here, J is the mean intensity of the interstellar radiation field being scattered, which we represented as the sum of three grey bodies

$$J(\nu_0) = \frac{2h\nu_0^3}{c^2} \left[\frac{1}{\exp(h\nu_0/kT_{\text{CMB}}) - 1} + \frac{\mathcal{N}_{\text{SL}}}{\exp(h\nu_0/kT_{\text{SL}}) - 1} + \frac{\mathcal{N}_{\text{IR}}}{\exp(h\nu_0/kT_{\text{IR}}) - 1} \right] \quad (32)$$

where h is the Planck constant, and k is the Boltzmann constant.

For FSR, the emission coefficient for photons of frequency ν is given by

$$\epsilon_\nu(r, \nu) = \frac{h\nu}{4\pi} \left[\frac{\rho_{\text{dm}}(r)}{m_{\text{dm}}} \right]^2 \frac{d\langle \sigma v \rangle_{\text{FSR}}}{d\nu}. \quad (33)$$

with each annihilation event yielding a photon spectrum given by

¹ Energy radiated per unit volume per unit frequency per unit time per unit solid angle.

Model	K_0 [cm ² s ⁻¹]	δ
MIN	7.06×10^{26}	0.46
MED (canonical)	1.67×10^{25}	0.70
MAX	7.69×10^{23}	0.85

Table 1. Three different models of the diffusion coefficient proposed by Donato et al. (2004), following the parameterization $K(\gamma) = K_0 \gamma^\delta$.

Model	\mathcal{N}_{SL} $T_{\text{SL}} = 3481$ K	\mathcal{N}_{IR} $T_{\text{IR}} = 40.6$ K
ISRF (I)	1.7×10^{-11}	7.0×10^{-5}
Canonical	2.7×10^{-12}	7.0×10^{-5}
ISRF (II)	8.9×10^{-13}	1.3×10^{-5}

Table 2. Normalization of the grey-body models describing the interstellar radiation field, adopted from Cirelli & Panci (2009).

$$\frac{d\langle\sigma v\rangle_{\text{FSR}}}{d\nu} = \langle\sigma v\rangle_{e^\pm} \frac{\alpha}{\pi} \frac{\kappa^2 - 2\kappa + 2}{\nu} \ln \left[\left(\frac{2m_{\text{dm}}}{m_e} \right)^2 (1 - \kappa) \right] \quad (34)$$

where α is the fine-structure constant and $\kappa = h\nu/m_{\text{dm}}c^2$ (see e.g. Peskin & Schroeder 1995).

2.5 Astrophysical parameters

The emission coefficient associated to final-state radiation is fully specified by the initial energy and injection rate of the electron-positron pairs, related to the nature of the dark matter particle (mass and cross-section) and the parameters describing the density profile of the Galactic halo. In contrast, the photon intensity from the synchrotron and ICS emission also depends on the astrophysical parameters that determine the propagation and energy losses of the relativistic particles. We will first define a canonical model based on observations of the Milky Way and then investigate the effect of each individual component by varying the values of the adopted parameters. In all cases, we calculate the electron-positron spectrum as described in expression (10), and then estimate the photon intensity according to expression (24).

Our canonical model assumes a dark matter density profile with $\alpha = 1$ (Navarro et al. 1997), $r_s = 17$ kpc and $\rho_s c^2 = 0.35$ GeV cm⁻³, consistent with dynamical models of the Milky Way (e.g. Dehnen & Binney 1998; Klypin et al. 2002). The virial mass of the Galaxy is thus $10^{12} M_\odot$, and the local dark matter density is $\rho_{\text{dm}}(r_\odot) c^2 = 0.3$ GeV cm⁻³. The ISM is mainly composed of neutral hydrogen atoms ($X_{\text{ion}} = 0$) with number density $\rho_g/m_p \sim 1$ cm⁻³ (Dehnen & Binney 1998; Ferrière 2001; Robin et al. 2003), and it is permeated by a tangled magnetic field whose intensity is $B \sim 6$ μ G throughout the Galaxy (Ferrière 2001; Beck 2001; Ascasibar & Díaz 2010).

Apart from the canonical model, we consider the effect that the magnetic field, the diffusion coefficient, and the interstellar radiation field have on the synchrotron and ICS emission. The intensity of the magnetic field B is varied from 1 to 100 μ G. For the diffusion coefficient (see equation 2), we consider the three models discussed by Donato et al. (2004) and summarized in Table 1. We will also use three different models of the ISRF (adopted from Cirelli & Panci 2009) where the photon intensity is represented by three grey-body

α	$\rho_s c^2$ [GeV cm ⁻³]	r_s [kpc]
0.00	2.346	8.64
0.20	1.737	9.56
0.50	1.042	11.41
0.70	0.702	13.08
1.00	0.349	16.67
1.20	0.197	20.33
1.25	0.169	21.49
1.50	0.066	29.81
1.70	0.025	42.57
1.90	0.006	70.30

Table 3. Characteristic density and radius of the dark matter density profile (22) as a function of its asymptotic logarithmic inner slope α .

components (see equations 12 and 32). The normalizations and effective temperatures of the light emitted by the Galactic stars and dust are quoted in Table 2.

Most importantly, we also investigate the effect of the inner slope of dark matter density profile on the production rate of electron-positron pairs. We vary the inner logarithmic slope α from 0.5 to 1.5. When varying α we also modify the characteristic density and radius in expression (22) so that the dark matter density at the solar radius is equal to 0.3 GeV cm⁻³ and the virial mass of the Galaxy is $10^{12} M_\odot$. The appropriate values of ρ_s and r_s are quoted in Table 3 for several values of the inner logarithmic slope α .

3 OBSERVATIONAL DATA

In order to constrain the production of relativistic electrons and positrons in the Milky Way, we consider observations of the whole sky at very different wavelengths. More precisely, the Haslam map in the radio band, the 5 WMAP channels at microwave wavelengths, and 12 energy bins of the Fermi LAT observations in the gamma-ray regime. The Haslam and WMAP maps are dominated by synchrotron emission, whereas Fermi traces ICS and FSR.

The Haslam 408 MHz radio continuum all-sky map (Haslam et al. 1981, 1982) combines data from four different surveys. The data were obtained from the archives of the NCSA ADIL in equatorial 1950 coordinates, and they were subsequently processed further in the Fourier domain to mitigate baseline striping and strong point sources. For the WMAP data, we take the full-resolution coadded temperature maps for each of the 5 frequency bands (23, 33, 41, 61, and 94 GHz) corresponding to the 7-year observations (Jarosik et al. 2011). The Fermi gamma-ray maps were computed by Dobler et al. (2010) from all “Class 3” (diffuse) photon events in the first-year data release. We use the 12 logarithmically-spaced frequency bands, from 0.3 to 300 GeV, of the smoothed maps without point source subtraction.

Since we are interested in a spherically-symmetric component, we may follow a simple, conservative procedure in order to mask the emission from the Galactic disk and individual point sources without relying on any particular foreground model. For each frequency, we compute the average intensity $I(\theta)$ in 180 bins as a function of the angular separation θ from the Galactic centre. We also estimate the

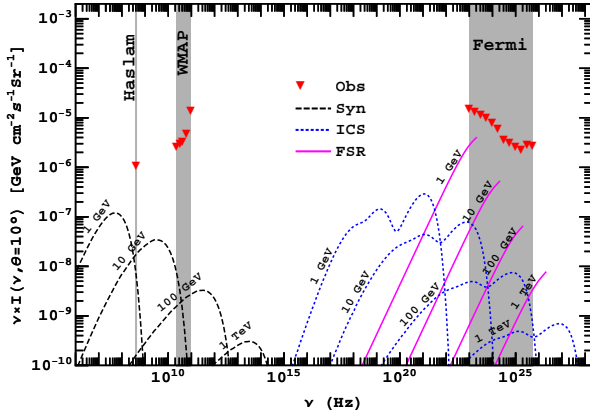


Figure 1. Theoretical photon spectra of synchrotron radiation (dashed black lines), ICS (dotted blue lines) and FSR (solid magenta lines) for our canonical model with $\langle \sigma v \rangle_{e\pm} = 3 \times 10^{-26} \text{ cm}^3 \text{ s}^{-1}$ and different injection energies, evaluated at 10° from the Galactic centre. Grey bands illustrate the frequency ranges of Haslam, WMAP and Fermi. The observational data at $\theta = 10^\circ$ are plotted as red triangles.

standard deviation $\sigma(\theta)$ within each bin, as well as the average standard deviation

$$\sigma_{\text{ave}} = \frac{\sum_{i=1}^n \sigma(\theta_i)}{n}, \quad (35)$$

where $n = 180$ is the total number of the bins. We then start an iterative procedure, where all pixels more than $3\sigma_{\text{ave}}$ away from $I(\theta)$ are discarded until convergence is achieved.

This method seems to correctly identify and remove the most obvious structures in all but the two highest-energy Fermi bands, where the photon statistics is so poor that it is extremely difficult to distinguish diffuse emission from individual point sources. For these two bands, we opted to use the original average intensity $I_0(\theta)$ without applying any mask. Raw intensity maps, masked residual maps, i.e. $I - I(\theta)$, and the average intensity $I(\theta)$ for each wavelength are shown in Figures A1, A2, and A3 of Appendix A. Numeric values of $I_0(\theta)$, $I(\theta)$, and $\sigma(\theta)$ are quoted in Tables A1, A2, A3, and A4.

Besides these observational data, we also consider the energy spectra of cosmic-ray electrons and positrons in the solar neighbourhood; in particular, we use the combined electron+positron spectrum measured by the Fermi (Ackermann et al. 2010b) and HESS (Aharonian et al. 2008) collaborations, as well as the positron-only spectrum determined from Fermi data (Ackermann et al. 2012). For PAMELA, we combine the electron-only spectrum obtained by Adriani et al. (2011) with the positron fraction discussed in Adriani et al. (2010) in order to derive the positron spectrum.

4 CONSTRAINTS ON THE DARK MATTER CROSS-SECTION

Once the emission from the galactic disc and the most prominent point sources is excluded, the remaining spherically-averaged component can be used to place upper limits on

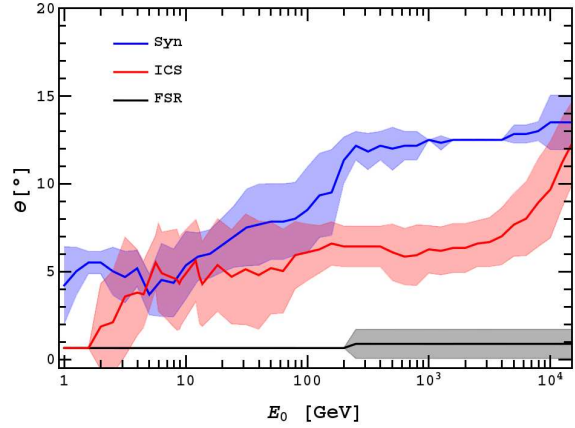


Figure 2. Angular separation θ that provides the upper limits for synchrotron, ICS and FSR emission. Lines and shadowed regions show the average and standard deviation across different wavelength channels, respectively.

the cross-section for dark matter annihilation into electron-positron pairs.

First of all, model intensities are computed according to the scheme described in Section 2. We consider the injection energy (i.e. the mass of the dark matter particle) as a free parameter and investigate values of the initial Lorentz factor γ_0 between 2×10^3 and 2×10^7 , corresponding to injection energies $E_0 = \gamma_0 m_e c^2$ from 1 GeV to 10 TeV. As an example, Figure 1 displays the results of our canonical Milky Way model for the synchrotron, inverse Compton, and final-state radiation contributions to the photon intensity at 10° from the Galactic centre, assuming a dark matter annihilation cross-section of $\langle \sigma v \rangle_{e\pm} = 3 \times 10^{-26} \text{ cm}^3 \text{ s}^{-1}$.

One can readily see that the Haslam radio map will be most sensitive to synchrotron emission by particles with an initial energy between 1 and 10 GeV, whereas WMAP data will cover the range $E_0 \sim 10 - 100$ GeV. On the other hand, the gamma rays observed by the Fermi LAT will constrain the maximum ICS and FSR emission allowed. The final-state radiation is sharply peaked at the injection energy, and it traces values of E_0 between 1 GeV and 1 TeV. The inverse Compton spectrum is broader, and it features three distinct emission peaks, due to the scattering of CMB, starlight, and infrared photons. It is best suited to probe injection energies between 10 and 100 GeV, although the maximum intensity is always much smaller than the FSR peak, and therefore the associated constraints are going to be weaker.

Since the value of the annihilation cross-section only sets the normalization of the spectra, and it does not alter its shape, it is relatively easy to set an upper limit by imposing that the model intensities do not exceed the observed values (red triangles in Figure 1) at *any* angular separation θ . Not surprisingly, the tightest constraint will always be provided by a small value of θ , i.e. close to the Galactic centre. The dark matter density, and thus the injection rate, are higher there than anywhere else in the Galaxy. However, the observed intensity also reaches a maximum at $\theta = 0$, and particles may diffuse from their injection point, effectively smoothing the density cusp. The angle that sets the maximum normalization that would be compatible with the observations (i.e. the upper limit of $\langle \sigma v \rangle_{e\pm}$) is plotted

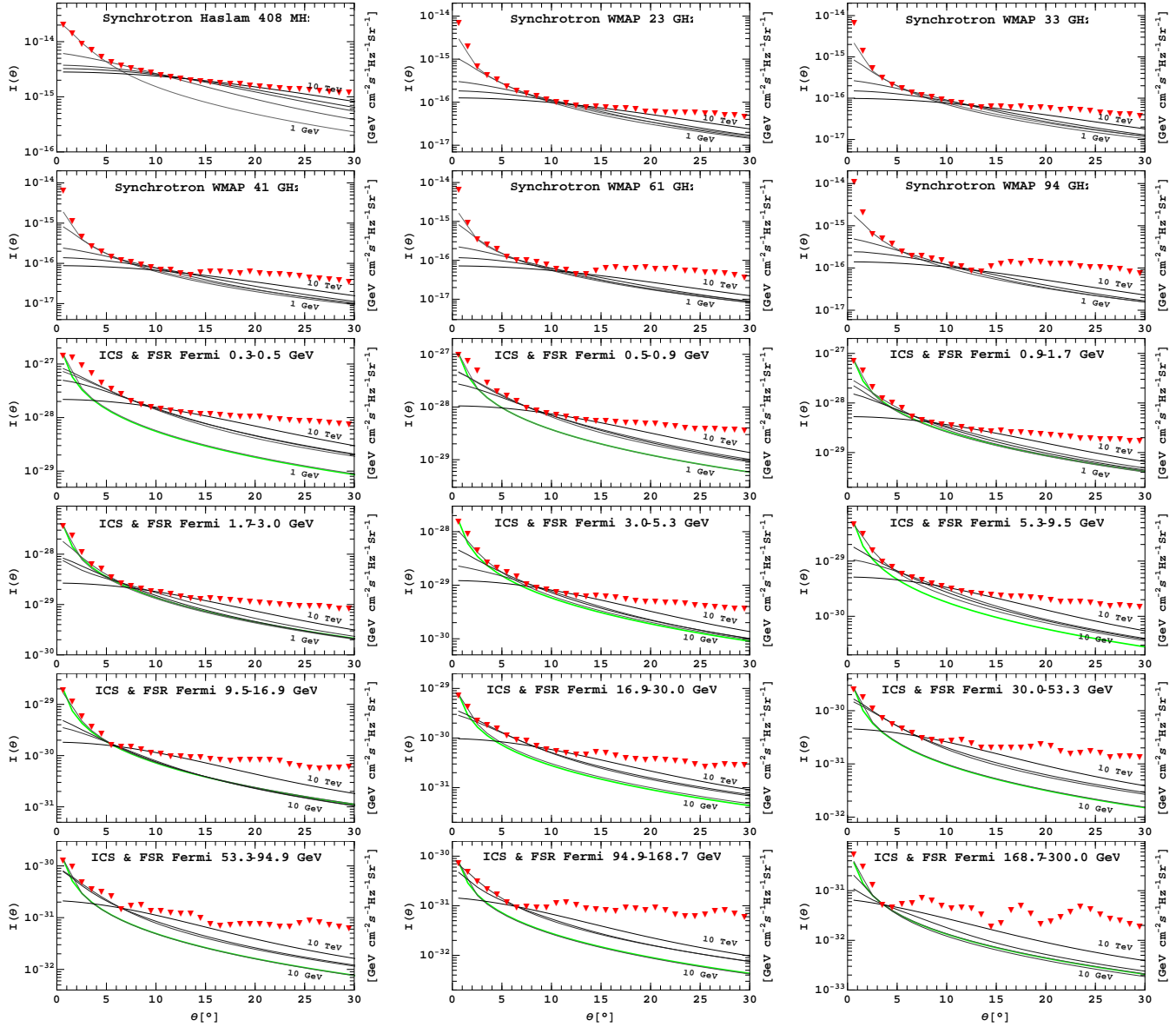


Figure 3. Surface brightness profiles of synchrotron, ICS, and FSR as a function of the angular separation θ from the Galactic centre. Red triangles correspond to the mean observational intensity after discarding the contribution of the Galactic disk and prominent point sources as discussed in Section 3. Theoretical profiles are normalized to the maximum value of the annihilation cross-section (see Figure 4) allowed by these data. The angular separation that provides the tightest constraint – i.e. the tangent point between models and observations – is depicted in Figure 2. For synchrotron and ICS emission, the intensities obtained for the canonical Milky Way model are expressed in grey to black lines, where a darker colour represents a higher value of the injection energy E_0 . The normalized intensity of FSR, shown as a green solid line, does not depend on E_0 .

in Figure 2, and the predicted surface brightness profiles of synchrotron, ICS, and FSR emission, normalized according to such prescription, are plotted in Figure 3 together with the observational data.

Final-state radiation is produced at the very moment of pair creation, and thus it directly traces the positron injection profile, which is, in turn, proportional to the square of the dark matter density. Therefore, the intensity of the FSR emission does not depend on the injection energy of the particles or any astrophysical parameter other than the inner logarithmic slope α of the dark matter density profile. For this reason, the normalized surface brightness profiles of FSR depicted in Figure 3 do *not* depend on E_0 . In our canon-

ical model (where $\alpha = 1$), and even more so if $\alpha > 1$, the tightest constraints on the final-state radiation come from the very centre of the Galaxy ($\theta < 1^\circ$).

For synchrotron and ICS emission, particle diffusion makes the intensity profile shallower, especially at high injection energies. In general, one can say that photons of a given frequency trace electrons and positrons within a certain energy range. If that range is close to E_0 , these particles would have just been injected, and therefore the effects of particle propagation should be small, whereas, for large values of E_0 , these electrons and positrons would have traveled a significant distance from the point of injection, and the surface brightness profile will become considerably shallower.

This trend is indeed evident in Figure 3: surface brightness profiles become progressively shallower as one moves from $E_0 = 1$ GeV to 10 TeV, and the effect is more pronounced for those channels that trace low-energy particles, i.e. Haslam, WMAP, and the lowest-energy Fermi bands. In the most extreme cases, diffusion keeps the electron-positron spectrum (and the ensuing intensity) roughly constant within the innermost $10 - 20^\circ$. For inverse Compton scattering, the tightest constraints on the annihilation cross-section come from $\theta \sim 5^\circ$ at all but the highest injection energies, whereas for synchrotron emission the optimal angle increases steadily from 5 to 15° (see Figure 2).

In addition to the photons arriving from the centre of the Milky Way, the dark matter annihilation cross-section $\langle\sigma v\rangle_{e^\pm}$ is also strongly constrained by the observed abundance of relativistic electrons and positrons in the solar neighbourhood. In particular, we consider the recent measurements of the *positron* spectrum by the Fermi collaboration (Ackermann et al. 2012) and the PAMELA experiment. The latter data have not been published as such in the literature, but they can be trivially derived from the quoted positron fraction (Adriani et al. 2010) and electron spectrum (Adriani et al. 2011). Since the positron fraction is of the order of 10 percent or less at the energies below ~ 10 GeV, the constraints from the positron-only spectrum will be much tighter than those derived from the combined electron+positron data. For the sake of comparison, we also show these for PAMELA (Adriani et al. 2011), Fermi (Ackermann et al. 2010b), and HESS (Aharonian et al. 2008). Note that, in the latter case, the measurements are able to probe higher (\sim TeV) energies, but it is not possible to discriminate between the electron and positron signatures.

Our constraints are derived by imposing that the predicted amount of electrons and/or positrons does not exceed the observed values for *any* Lorentz factor γ . Given the energy dependence of the observed spectrum, $\left[\frac{dn}{dE}\right]_{\text{obs}} \sim E^{-3}$, and the energy losses, $b(E) \sim E^2$, the most restrictive constraint comes from the spectrum near the injection energy, where propagation can be safely neglected and $\left[\frac{dn}{dE}\right]_{\text{model}} \approx \frac{Q_0}{b} \propto E^{-2}$. The maximum production rate allowed by the data can then be expressed as

$$Q_0(r_\odot) < b(\gamma_0) \left[\frac{dn}{dE}\right]_{\text{obs}}(\gamma_0), \quad (36)$$

and one arrives to the condition

$$\langle\sigma v\rangle_{e^\pm}(\gamma_0) < \left[\frac{m_{\text{dm}}}{\rho_{\text{dm}}(r_\odot)}\right]^2 b(\gamma_0) \left[\frac{dn}{dE}\right]_{\text{obs}}(\gamma_0) \quad (37)$$

in order not to overproduce the observed signal.

The results are plotted in Figure 4, together with the upper limits on the dark matter annihilation cross-section derived from the comparison of the predicted synchrotron, ICS and FSR emission, assuming our canonical Milky Way model for particle propagation, with multi-wavelength observations by Haslam, WMAP, and Fermi. As can be readily seen in the figure, the tightest constraints are provided by the final-state radiation from the Galactic centre for injection energies above 20 – 30 GeV, whereas the positron spectrum in the solar neighbourhood limits the production cross-section at lower energies. The constraints obtained from synchrotron and inverse Compton scattering are much weaker,

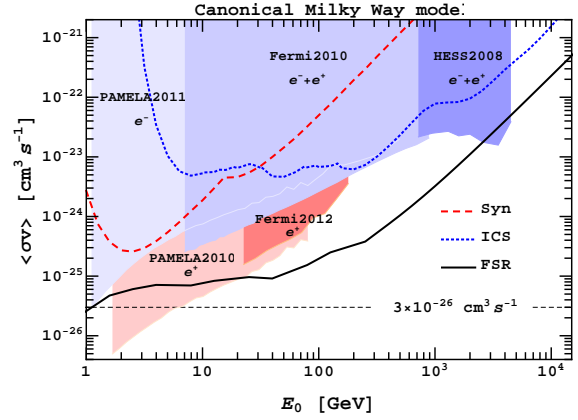


Figure 4. Upper limits on the dark matter annihilation cross-section derived by comparing the predicted synchrotron (red dashed line), ICS (blue dot-dashed line) and FSR (black solid line) emission with multi-wavelength observational data. The areas shaded in blue show the constraints obtained from the measurements of the combined electron+positron spectrum at the solar neighbourhood by PAMELA, Fermi and HESS. The upper limits obtained from the positron spectrum are shown by the red areas. The horizontal dotted line indicates the value $\langle\sigma v\rangle_{e^\pm} = 3 \times 10^{-26} \text{ cm}^3 \text{ s}^{-1}$.

by about one order of magnitude, and similar to the upper limits associated to the combined electron and positron spectrum in the solar neighbourhood.

The typical value for thermal relics, $\langle\sigma v\rangle_{e^\pm} = 3 \times 10^{-26} \text{ cm}^3 \text{ s}^{-1}$, is ruled out for particle masses lighter than a few GeV. Both particle physics processes and astrophysical boost factors have previously been advocated to increase the current annihilation rate in the Milky Way by more than a factor of 10 with respect to the early universe. According to Figure 4, such models are excluded for any dark matter candidate below the \sim TeV regime annihilating primarily into electron-positron pairs. Since our analysis involves a very conservative treatment of the astrophysical signal, merely excluding the emission from the disk and prominent point sources, it is expected that a deeper understanding of the astrophysical sources of electrons and positrons would make possible to probe the interesting region of the parameter space below $\langle\sigma v\rangle_{e^\pm} = 3 \times 10^{-26} \text{ cm}^3 \text{ s}^{-1}$.

5 EFFECT OF THE ASTROPHYSICAL PARAMETERS

All the constraints represented in Figure 4 are based on the ‘canonical’ Milky Way model discussed in Section 2.5. One should note that the most stringent results are provided by the final-state radiation from the Galactic centre and the local positron spectrum. These observables directly trace the instantaneous injection rate, and therefore they do not depend on the propagation parameters. However, the surface brightness profiles of synchrotron and ICS emission are sensitive to the precise values adopted for the intensity of the magnetic field, the diffusion coefficient, and the interstellar radiation field. The inner logarithmic slope of dark matter density profile has a very strong impact on the injection rate close to the centre, and thus it affects all the tracers con-

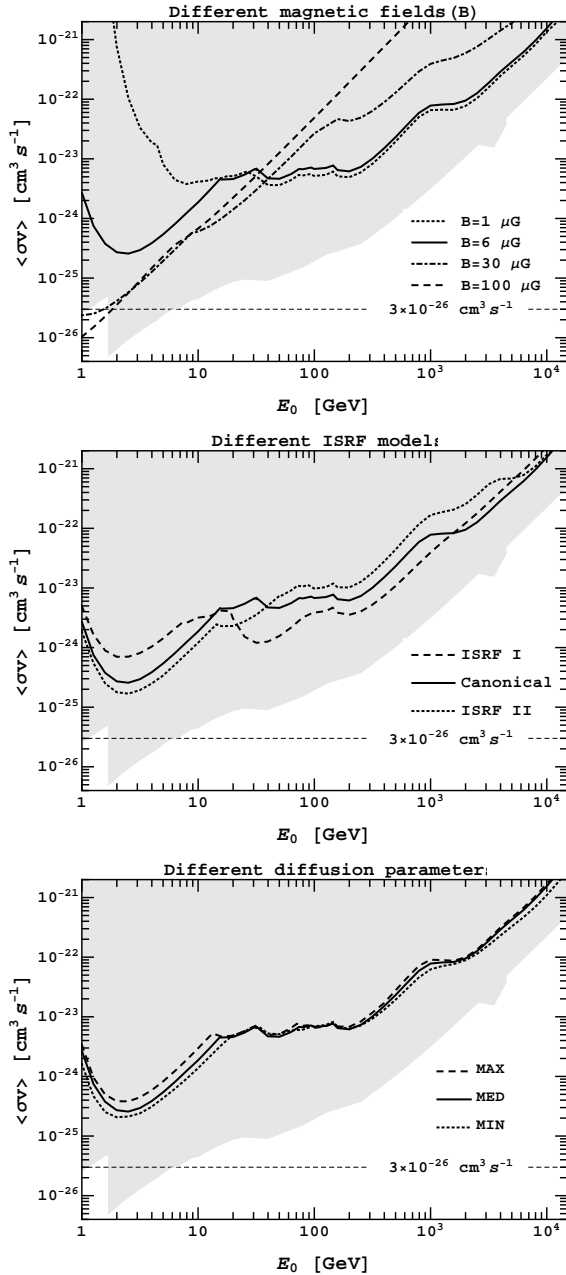


Figure 5. Upper limits on the dark matter annihilation cross-section from synchrotron and ICS, for different values of the magnetic field (top), interstellar radiation field (middle), and diffusion coefficient (bottom). Constraints from FSR and the local positron spectrum are indicated by the shaded area.

sidered in the present work except the positron spectrum in the solar neighbourhood.

Here we investigate the effect of the various astrophysical parameters of our propagation model on the upper limits obtained for the dark matter annihilation cross-section. As we did for the canonical model, we consider different initial energies E_0 from 1 GeV to 10 TeV and compare the predicted emission with the full observational data set, but now we vary each of the astrophysical parameters in turn in order to assess their influence on the results.

Let us start with the intensity of the magnetic field

B . This parameter plays an important role in the energy losses, and it sets the total amount of energy that is radiated away as synchrotron emission. The top panel on Figure 5 shows the upper limits derived by combining the constraints obtained from synchrotron and inverse Compton scattering. The results obtained $B = 1, 6$ (our canonical model), 30 and 100 μG are plotted as dotted, solid, dash-dotted, and dashed lines, respectively. All the other constraints (FSR and local positron spectrum) are independent of B , and are shown by the shaded area.

Synchrotron constraints are most important at the lowest injection energies ($E_0 \sim 1 - 30$ GeV), while the upper limits at higher initial energies (from ~ 30 GeV to 10 TeV) are due to ICS in the gamma-ray regime. The intensity of the magnetic field affects both processes in an opposite way: for low values of the magnetic field, all energy is lost by inverse Compton scattering, and synchrotron emission is almost irrelevant; as one increases the value of B , synchrotron constraints become more important at the expense of ICS emission. In the most extreme case ($B = 100 \mu\text{G}$), gamma-ray constraints are negligible, and the upper limits derived from synchrotron radiation are well approximated by a pure power law. For any value of the magnetic field, the upper limits derived from FSR and the positron spectrum are always more stringent than those derived from synchrotron and ICS.

In the middle panel of Figure 5, we investigate the upper limits of synchrotron and ICS for different models of the interstellar radiation field. As mentioned in Section 2.5, we adopted the parameterization proposed by Cirelli & Panci (2009) in terms of three black-body components. The temperatures and normalizations of each component are summarized in Table 2. The effect of the ISRF is similar to that of the magnetic field, but in the opposite direction: a higher photon density results in a larger amount of energy being lost by inverse Compton scattering rather than synchrotron emission. Nevertheless, for reasonable values of the model parameters, the upper limits on $\langle\sigma v\rangle$ do not vary by more than a factor of three.

As shown on the bottom panel of Figure 5, the effect of the diffusion coefficient is even smaller. The upper limits are slightly more stringent when the electrons and positrons are allowed to travel a shorter distance from the place where they were injected, but the difference between the three propagation models discussed by Donato et al. (2004) is barely noticeable.

Thus, we conclude that our results are not severely affected by the astrophysical uncertainties associated to particle propagation. In particular, synchrotron and inverse Compton constraints are weaker than the upper limits from final-state radiation and the local positron spectrum for any value of the magnetic field, the interstellar radiation field, or the diffusion coefficient.

This conclusion is also valid for any value of the inner slope α of the dark matter density profile, but this parameter plays a very important role in setting the actual constraints on $\langle\sigma v\rangle$. We have investigated several values in the interval $0 < \alpha < 2$ (the appropriate values of ρ_s and r_s are quoted in Table 3), and we report in Figure 6 the upper limits obtained from the comparison of the predicted final-state radiation, synchrotron, and inverse Compton scattering emission for $\alpha = 0.50, 1.00, 1.25$, and 1.50 with our multi-wavelength

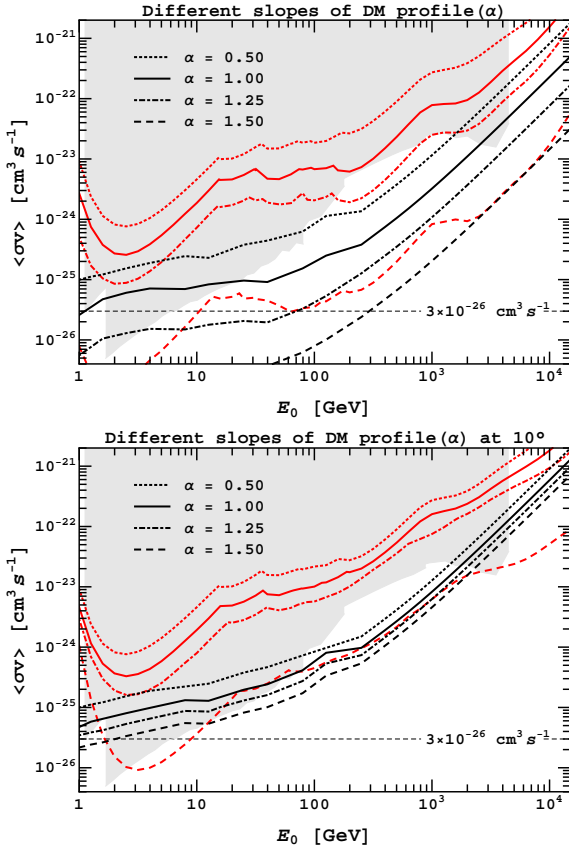


Figure 6. Upper limits on the dark matter annihilation cross-section for different values of the inner logarithmic slope α of the dark matter density profile. On the top panel, the constraints are derived from the angle that provides the most stringent limit (see Figure 2 for the canonical case $\alpha = 1$), whereas all the constraints on the bottom panel are obtained from the observed emission at $\theta = 10^\circ$ from the Galactic centre. In both cases, black and red lines represent the limits associated to FSR and Synchrotron+ICS emission, respectively. The constraints from the local positron spectrum (independent on α) are shown by the shadowed areas.

observational data set. Results for FSR and the combination of synchrotron and ICS emission are plotted separately. Constraints from the local positron spectrum are independent of α and are shown as a solid area.

The top panel of the figure shows the upper limits obtained by the same procedure applied to the canonical model, i.e. choosing the angular separation θ that provides the tightest constraint. Not surprisingly, larger values of α result in lower values of θ . The constraints from FSR and Synchrotron+ICS emission come from innermost 1° for $\alpha > 0.5$ and $\alpha > 1.25$, respectively.

Since the particle production rate near the centre of the Milky Way increases dramatically with the value of the inner slope of the density profile, this is, by far, the most relevant astrophysical parameter. For $\alpha > 1.25$, the upper limits from final-state radiation are always stronger than the constraints provided by the local positron spectrum, and they rule out a cross-section larger than $3 \times 10^{-26} \text{ cm}^3 \text{ s}^{-1}$ for any dark matter candidate lighter than ~ 100 GeV. On the contrary, if the dark matter density profile of the Milky Way was shallow, with a logarithmic slope $\alpha < 0.50$, the

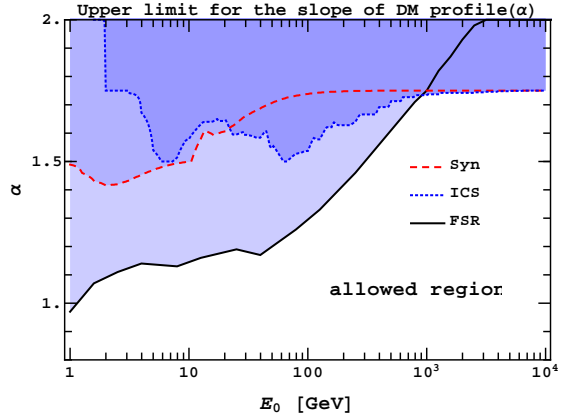


Figure 7. Upper limits on the inner logarithmic slope of dark matter density profile α , obtained by imposing that FSR from the Galactic centre does not overproduce the observed signal (according to the Fermi data) for a thermal dark matter relic (i.e. $\langle\sigma v\rangle_{e^\pm} = 3 \times 10^{-26} \text{ cm}^3 \text{ s}^{-1}$).

positron spectrum in the solar neighbourhood would provide the most stringent limits on dark matter annihilation.

One may remove the dependency of the results on the precise shape of the dark matter density profile by fixing $\theta = 10^\circ$ when comparing model predictions with observational data. As shown in the bottom panel of Figure 6, we find, in agreement with previous work (e.g. Serpico & Zaharijas 2008; Ackermann et al. 2012), that the uncertainty associated to the precise value of α reduces to about a factor of 2 when the comparison is restricted to the photon intensity at $\theta = 10^\circ$. While this is therefore a good choice when the goal is to provide a conservative upper limit on the dark matter annihilation cross-section, we would like to stress that any prior knowledge of the dark matter density profile may lead to much stronger constraints if the inner slope was steeper than $\alpha = 1$, as evidenced in the upper panel.

6 CONSTRAINTS ON THE INNER SLOPE OF THE DENSITY PROFILE

As pointed out in Ascasibar et al. (2006), the photons from the central region of the Galaxy contain information on *both* the dark matter annihilation cross-section and the shape of the density profile. By assuming a given value of the cross-section, one can constrain the value of α from the total intensity and the morphology of the observed surface brightness.

In this work, we will focus only on the total intensity from the central bin (i.e. one degree around the Galactic centre) in order to derive a robust upper limit. More detailed constraints could be obtained from the shape of the surface brightness profiles at different wavelengths once the astrophysical contribution is adequately subtracted. We set the dark matter annihilation cross-section into electron-positron pairs to the value expected for a thermally-produced relic, $\langle\sigma v\rangle_{e^\pm} = 3 \times 10^{-26} \text{ cm}^3 \text{ s}^{-1}$, and compute the value of α for which the predicted final-state radiation rises above the observed level.

The corresponding upper limit is plotted in Figure 7 as a function of the initial energy E_0 associated to the mass of dark matter candidate. Our results show that, for a thermal

relic with $m_{\text{dm}} < 100$ GeV, the dark matter density profile of the Milky Way *must* be shallower than $\alpha \sim 1.3$ in order not to overproduce the observed signal. It is worth noting that, since FSR only depends on the injection rate, our constraint on the inner logarithmic slope α is independent on the other astrophysical parameters. Moreover, the fact that we are considering the total gamma-ray emission, without taking into account the contribution of astrophysical origin, implies that this is a conservative upper limit, and therefore we can conclude that, if dark matter particles annihilate primarily into electrons and positrons (or, more generally, any lepton pair), any scenario where the Milky way features a steep density profile (due to e.g. adiabatic contraction) may be firmly ruled out.

7 SUMMARY AND CONCLUSIONS

We have investigated the constraints on the dark matter annihilation cross-section into electron-positron pairs by comparing the predictions of an analytic model of particle propagation with a multi-wavelength set of observational data obtained from the literature. We have compared the expected emission from synchrotron radiation, inverse Compton scattering and final-state radiation within the Milky Way with 18 maps of the sky at different frequencies: the Haslam radio map at 408 MHz, the 7-year data from the Wilkinson Microwave Anisotropy Probe (WMAP) in its 5 bands (23 GHz, 33 GHz, 41 GHz, 61 GHz, and 94 GHz), and gamma-ray maps from the Fermi Large Area Telescope (LAT) binned in 12 different channels (from 0.3 to 300 GeV). A straightforward statistical criterion has been followed in order to mask the most obvious astrophysical signals (i.e. the emission from the galactic disc and prominent point sources), and observational upper limits are derived from the remaining spherically-symmetric component. In addition, we have also imposed that the predicted abundance of electrons and positrons in the solar neighbourhood does not exceed the measurements by PAMELA, HESS and Fermi. Our main results can be summarized as follows:

(i) The constraints from synchrotron and inverse Compton emission are always weaker than those from final-state radiation from the Galactic centre and the positron spectrum in the solar neighbourhood. This result is valid for all the values of the magnetic field, diffusion coefficient, and models of the interstellar radiation field that we have considered.

(ii) If the density profile of the Milky Way halo is steep ($\alpha > 1$), the annihilation cross-section is most tightly constrained by final-state radiation, and the exact value of inner logarithmic slope plays a crucial role in the upper limit on $\langle\sigma v\rangle_{e\pm}$. This scenario is hardly consistent with any dark matter candidate lighter than ~ 100 GeV and $\langle\sigma v\rangle_{e\pm} = 3 \times 10^{-26} \text{ cm}^3 \text{ s}^{-1}$.

(iii) If the density profile of the Milky Way halo is relatively shallow ($\alpha \leq 1$), the upper limit on the cross-section is set by the local positron spectrum for low values of the injection energy. Combining both types of messenger (photons and positrons) is thus of the utmost importance in this case. Considering the positron spectrum separately makes possible to rule out cross-sections above $3 \times 10^{-26} \text{ cm}^3 \text{ s}^{-1}$ for dark matter particles lighter than a few GeV.

Let us conclude by noting that the current upper limits are close to – or have just reached – the expected annihilation cross-section for a thermal relic. A better understanding of the production of positrons and gamma rays by astrophysical sources should thus lead to the detection of an indirect signal from dark matter annihilation into electrons and positrons, providing at the same time an exquisite probe of the distribution of dark matter in the innermost regions of the Milky Way halo. Otherwise, the most straightforward version of the leptophilic dark matter scenario would be ruled out completely.

ACKNOWLEDGMENTS

Funding for this work has been provided by the DFG Research Grant AS 312/1-1 (Germany). MW also acknowledges support from Brückenprogramm of Universität Potsdam (Germany) and would like to thank V. Müller and J.C. Muñoz-Cuartas for useful discussions, as well as F. Breitling and J. Klar for their help with programming questions. YA is supported by grant AYA2010-21887-C04-03 from the former *Ministerio de Ciencia e Innovación* (Spain), as well as the *Ramón y Cajal* programme (RyC-2011-09461), now managed by the *Ministerio de Economía y Competitividad* (fiercely cutting back on the Spanish scientific infrastructure).

REFERENCES

- Abazajian K., Fuller G. M., Tucker W. H., 2001, *ApJ*, 562, 593
- Abazajian K. N., Agrawal P., Chacko Z., Kilic C., 2010, *JCAP*, 11, 41
- Abdo A. A., Ackermann M., Ajello M., et al. ., 2010, *ApJ*, 712, 147
- Abramowski A., Acero F., Aharonian F., Zechlin H.-S., H.E.S.S. Collaboration 2011, *Astroparticle Physics*, 34, 608
- Acciari V. A., Arlen T., Aune T., Beilicke M., Benbow W., Boltuch D., Bradbury S. M., 2010, *ApJ*, 720, 1174
- Ackermann M., Ajello M., Albert A., et al. [The Fermi-LAT collaboration] ., 2011, *Physical Review Letters*, 107, 241302
- Ackermann M., Ajello M., Allafort A., et al. [The Fermi-LAT collaboration] ., 2012, *Physical Review Letters*, 108, 011103
- Ackermann M., Ajello M., Atwood W. B., et al. [The Fermi-LAT collaboration] ., 2010a, *JCAP*, 5, 25
- Ackermann M., Ajello M., Atwood W. B., et al. [The Fermi-LAT collaboration] ., 2010b, *Phys. Rev. D*, 82, 092004
- Ackermann M., Ajello M., Atwood W. B., et al. [The Fermi-LAT collaboration] ., 2012, *ArXiv e-prints*
- Adriani O., Barbarino G. C., Bazilevskaya G. A. and et al. [PAMELA collaboration] ., 2011, *Physical Review Letters*, 106, 201101
- Adriani O., Barbarino G. C., Bazilevskaya G. A., et al. [PAMELA collaboration] ., 2009a, *Nature*, 458, 607
- Adriani O., Barbarino G. C., Bazilevskaya G. A., et al. [PAMELA collaboration] ., 2009b, *Physical Review Letters*, 102, 051101

- Adriani O., Barbarino G. C., Bazilevskaya G. A., et al. [PAMELA collaboration] ., 2010, *Astroparticle Physics*, 34, 1
- Aharonian F., Akhperjanian A. G., Barres de Almeida U., et al. [HESS collaboration] ., 2008, *Physical Review Letters*, 101, 261104
- Aharonian F., Akhperjanian A. G., Bazer-Bachi A. R., et al. [HESS collaboration] ., 2006, *Physical Review Letters*, 97, 221102
- Aloisio R., Blasi P., Olinto A. V., 2004, *JCAP*, 5, 7
- Ascasibar Y., Díaz A. I., 2010, *MNRAS*, 404, 275
- Ascasibar Y., Jean P., Boehm C., Knödseder J., 2006, *MNRAS*, 368, 1695
- Baltz E. A., Briot C., Salati P., Taillet R., Silk J., 2000, *Phys. Rev. D*, 61, 023514
- Baltz E. A., Edsjö J., 1999, *Phys. Rev. D*, 59, 023511
- Baltz E. A., Wai L., 2004, *Phys. Rev. D*, 70, 023512
- Barger V., Gao Y., Keung W.-Y., Marfatia D., Shaughnessy G., 2009, *Physics Letters B*, 678, 283
- Beacom J. F., Bell N. F., Bertone G., 2005, *Physical Review Letters*, 94, 171301
- Beacom J. F., Yüksel H., 2006, *Physical Review Letters*, 97, 071102
- Beck R., 2001, *Space Science Reviews*, 99, 243
- Bell N. F., Jacques T. D., 2009, *Phys. Rev. D*, 79, 043507
- Berezinsky V., Bottino A., Mignola G., 1994, *Physics Letters B*, 325, 136
- Bergström L., Bertone G., Bringmann T., Edsjö J., Taoso M., 2009, *Phys. Rev. D*, 79, 081303
- Bergström L., Bringmann T., Eriksson M., Gustafsson M., 2005a, *Physical Review Letters*, 95, 241301
- Bergström L., Bringmann T., Eriksson M., Gustafsson M., 2005b, *Physical Review Letters*, 94, 131301
- Bergström L., Edsjö J., Zaharijas G., 2009, *Physical Review Letters*, 103, 031103
- Bergström L., Hooper D., 2006, *Phys. Rev. D*, 73, 063510
- Bergström L., Ullio P., Buckley J. H., 1998, *Astroparticle Physics*, 9, 137
- Bernal N., Palomares-Ruiz S., 2010, *ArXiv1006.0477*
- Bertone G., 2010, *Particle Dark Matter : Observations, Models and Searches*. Cambridge University Press
- Bertone G., Cirelli M., Strumia A., Taoso M., 2009, *JCAP*, 3, 9
- Bertone G., Hooper D., Silk J., 2005, *Physics Reports*, 405, 279
- Blasi P., Olinto A. V., Tyler C., 2003, *Astroparticle Physics*, 18, 649
- Blumenthal G. R., Faber S. M., Flores R., Primack J. R., 1986, *ApJ*, 301, 27
- Blumenthal G. R., Gould R. J., 1970, *Reviews of Modern Physics*, 42, 237
- Boehm C., Ascasibar Y., 2004, *Phys. Rev. D*, 70, 115013
- Boehm C., Hooper D., Silk J., Casse M., Paul J., 2004, *Physical Review Letters*, 92, 101301
- Borriello E., Cuoco A., Miele G., 2009, *Phys. Rev. D*, 79, 023518
- Boyarsky A., den Herder J.-W., Neronov A., Ruchayskiy O., 2007, *Astroparticle Physics*, 28, 303
- Boyarsky A., Malyshev D., Neronov A., Ruchayskiy O., 2008, *MNRAS*, 387, 1345
- Boyarsky A., Ruchayskiy O., Markevitch M., 2008, *ApJ*, 673, 752
- Cesarini A., Fucito F., Lionetto A., Morselli A., Ullio P., 2004, *Astroparticle Physics*, 21, 267
- Chen C.-R., Takahashi F., 2009, *JCAP*, 2, 4
- Chen F., Cline J. M., Fradette A., Frey A. R., Rabideau C., 2010, *Phys. Rev. D*, 81, 043523
- Cholis I., Finkbeiner D. P., Goodenough L., Weiner N., 2009, *JCAP*, 12, 7
- Cholis I., Goodenough L., Weiner N., 2009, *Phys. Rev. D*, 79, 123505
- Cirelli M., Kadastik M., Raidal M., Strumia A., 2009, *Nuclear Physics B*, 813, 1
- Cirelli M., Panci P., 2009, *Nuclear Physics B*, 821, 399
- Cirelli M., Panci P., Serpico P. D., 2010, *Nuclear Physics B*, 840, 284
- Cline J. M., Frey A. R., Chen F., 2011, *Phys. Rev. D*, 83, 083511
- Colafrancesco S., 2004, *A&A*, 422, L23
- Colafrancesco S., Mele B., 2001, *ApJ*, 562, 24
- Colafrancesco S., Profumo S., Ullio P., 2006, *A&A*, 455, 21
- Crocker R. M., Bell N. F., Balázs C., Jones D. I., 2010, *Phys. Rev. D*, 81, 063516
- Dehnen W., Binney J., 1998, *MNRAS*, 294, 429
- Delahaye T., Böhm C., Silk J., 2012, *MNRAS*, 422, L16
- Delahaye T., Lineros R., Donato F., Fornengo N., Lavalle J., Salati P., Taillet R., 2009, *A&A*, 501, 821
- Dobler G., Finkbeiner D. P., Cholis I., Slatyer T., Weiner N., 2010, *ApJ*, 717, 825
- Donato F., Fornengo N., Maurin D., Salati P., Taillet R., 2004, *Phys. Rev. D*, 69, 063501
- Donato F., Maurin D., Brun P., Delahaye T., Salati P., 2009, *Physical Review Letters*, 102, 071301
- El-Zant A., Shlosman I., Hoffman Y., 2001, *ApJ*, 560, 636
- Essig R., Sehgal N., Strigari L. E., 2009, *Phys. Rev. D*, 80, 023506
- Essig R., Sehgal N., Strigari L. E., Geha M., Simon J. D., 2010, *Phys. Rev. D*, 82, 123503
- Ferrière K. M., 2001, *Reviews of Modern Physics*, 73, 1031
- Finkbeiner D. P., Weiner N., 2007, *Phys. Rev. D*, 76, 083519
- Fixsen D. J., 2009, *ApJ*, 707, 916
- Fornasa M., Pieri L., Bertone G., Branchini E., 2009, *Phys. Rev. D*, 80, 023518
- Fornengo N., Lineros R. A., Regis M., Taoso M., 2012, *JCAP*, 1, 5
- Galli S., Iocco F., Bertone G., Melchiorri A., 2009, *Phys. Rev. D*, 80, 023505
- Galli S., Iocco F., Bertone G., Melchiorri A., 2011, *Phys. Rev. D*, 84, 027302
- Ghisellini G., Guilbert P. W., Svensson R., 1988, *ApJ*, 334, L5
- Gondolo P., Silk J., 1999, *Physical Review Letters*, 83, 1719
- Grasso D., Profumo S., Strong A. W., et al. ., 2009, *Astroparticle Physics*, 32, 140
- Haslam C. G. T., Klein U., Salter C. J., Stoffel H., Wilson W. E., Cleary M. N., Cooke D. J., Thomasson P., 1981, *A&A*, 100, 209
- Haslam C. G. T., Salter C. J., Stoffel H., Wilson W. E., 1982, *A&AS*, 47, 1
- Hooper D., Ferrer F., Boehm C., Silk J., Paul J., Evans N. W., Casse M., 2004, *Physical Review Letters*, 93, 161302

- Hooper D., Goodenough L., 2011, *Physics Letters B*, 697, 412
- Hooper D., Linden T., 2011a, *Phys. Rev. D*, 83, 083517
- Hooper D., Linden T., 2011b, *Phys. Rev. D*, 84, 123005
- Hütsi G., Chluba J., Hektor A., Raidal M., 2011, *A&A*, 535, A26
- Ishiwata K., Matsumoto S., Moroi T., 2009, *Phys. Rev. D*, 79, 043527
- Jarosik N., Bennett C. L., Dunkley J., Gold B., Greason M. R., et al., 2011, *ApJS*, 192, 14
- Jeltema T. E., Kehayias J., Profumo S., 2009, *Phys. Rev. D*, 80, 023005
- Kanzaki T., Kawasaki M., Nakayama K., 2010, *Progress of Theoretical Physics*, 123, 853
- Klypin A., Zhao H., Somerville R. S., 2002, *ApJ*, 573, 597
- Lavalle J., 2010, *Phys. Rev. D*, 82, 083521
- Longair M. S., 1981, *High energy astrophysics: An Informal Introduction for Students of Physics and Astronomy*. Cambridge Univ. Press, Cambridge
- Malyshev D., Cholis I., Gelfand J., 2009, *Phys. Rev. D*, 80, 063005
- Mapelli M., Ferrara A., Pierpaoli E., 2006, *MNRAS*, 369, 1719
- Martinez G. D., Bullock J. S., Kaplinghat M., Strigari L. E., Trotta R., 2009, *JCAP*, 6, 14
- Mashchenko S., Couchman H. M. P., Wadsley J., 2006, *Nature*, 442, 539
- McQuinn M., Zaldarriaga M., 2011, *MNRAS*, 414, 3577
- Meade P., Papucci M., Strumia A., Volansky T., 2010, *Nuclear Physics B*, 831, 178
- Mertsch P., Sarkar S., 2009, *Physical Review Letters*, 103, 081104
- Morselli A., Lionetto A., Cesarini A., Fucito F., Ullio P., 2002, *Nuclear Physics B Proceedings Supplements*, 113, 213
- Navarro J. F., Frenk C. S., White S. D. M., 1997, *ApJ*, 490, 493
- Oh S., Brook C., Governato F., Brinks E., Mayer L., de Blok W. J. G., Brooks A., Walter F., 2010, *ArXiv1011.2777*
- Padmanabhan N., Finkbeiner D. P., 2005, *Phys. Rev. D*, 72, 023508
- Papucci M., Strumia A., 2010, *JCAP*, 3, 14
- Pato M., Pieri L., Bertone G., 2009, *Phys. Rev. D*, 80, 103510
- Peirani S., Mohayaee R., de Freitas Pacheco J. A., 2004, *Phys. Rev. D*, 70, 043503
- Peskin M. E., Schroeder D. V., 1995, *An Introduction to Quantum Field Theory*. Westview Press
- Picciotto C., Pospelov M., 2005, *Physics Letters B*, 605, 15
- Pinzke A., Pfrommer C., Bergström L., 2011, *Phys. Rev. D*, 84, 123509
- Porter T. A., Moskalenko I. V., Strong A. W., Orlando E., Bouchet L., 2008, *ApJ*, 682, 400
- Porter T. A., Strong A. W., 2005, in *International Cosmic Ray Conference Vol. 4 of International Cosmic Ray Conference*, A new estimate of the Galactic interstellar radiation field between 0.1um and 1000um. p. 77
- Pospelov M., Ritz A., 2007, *Physics Letters B*, 651, 208
- Pospelov M., Ritz A., Voloshin M., 2008, *Physics Letters B*, 662, 53
- Prada F., Klypin A., Flix J., Martínez M., Simonneau E., 2004, *Physical Review Letters*, 93, 241301
- Prantzos N., Boehm C., Bykov A. M., Diehl R., Ferrière K., Guessoum N., Jean P., Knoedseder J., Marcowith A., Moskalenko I. V., Strong A., Weidenspointner G., 2011, *Reviews of Modern Physics*, 83, 1001
- Profumo S., 2005, *Phys. Rev. D*, 72, 103521
- Profumo S., 2012, *Central European Journal of Physics*, 10, 1
- Profumo S., Ullio P., 2010, *ArXiv1001.4086*
- Regis M., 2008, *Physics Letters B*, 663, 250
- Regis M., Ullio P., 2008, *Phys. Rev. D*, 78, 043505
- Regis M., Ullio P., 2009, *Phys. Rev. D*, 80, 043525
- Rephaeli Y., 1979, *ApJ*, 227, 364
- Robin A. C., Reylé C., Derrière S., Picaud S., 2003, *A&A*, 409, 523
- Sánchez-Conde M. A., Cannoni M., Zandanel F., Gómez M. E., Prada F., 2011, *JCAP*, 12, 11
- Sánchez-Conde M. A., Prada F., Lokas E. L., Gómez M. E., Wojtak R., Moles M., 2007, *Phys. Rev. D*, 76, 123509
- Sarazin C. L., 1999, *ApJ*, 520, 529
- Serpico P. D., Zaharijas G., 2008, *Astroparticle Physics*, 29, 380
- Sizun P., Cassé M., Schanne S., 2006, *Phys. Rev. D*, 74, 063514
- Slatyer T. R., Padmanabhan N., Finkbeiner D. P., 2009, *Phys. Rev. D*, 80, 043526
- Springel V., White S. D. M., Frenk C. S., Navarro J. F., Jenkins A., Vogelsberger M., Wang J., Ludlow A., Helmi A., 2008, *Nature*, 456, 73
- Stoehr F., White S. D. M., Springel V., Tormen G., Yoshida N., 2003, *MNRAS*, 345, 1313
- Strigari L. E., Koushiappas S. M., Bullock J. S., Kaplinghat M., 2007, *Phys. Rev. D*, 75, 083526
- Strigari L. E., Koushiappas S. M., Bullock J. S., Kaplinghat M., Simon J. D., Geha M., Willman B., 2008, *ApJ*, 678, 614
- Tyler C., 2002, *Phys. Rev. D*, 66, 023509
- Ullio P., Bergström L., Edsjö J., Lacey C., 2002, *Phys. Rev. D*, 66, 123502
- Vincent A. C., Martin P., Cline J. M., 2012, *JCAP*, 4, 22
- Wechakama M., Ascasibar Y., 2011, *MNRAS*, 413, 1991
- Weidenspointner G., Skinner G., Jean P., Knödseder J., von Ballmoos P., Bignami G., Diehl R., Strong A. W., Cordier B., Schanne S., Winkler C., 2008, *Nature*, 451, 159
- Wood M., Blaylock G., Bradbury S. M., et al., 2008, *ApJ*, 678, 594
- Yin P.-F., Yuan Q., Liu J., Zhang J., Bi X.-J., Zhu S.-H., Zhang X., 2009, *Phys. Rev. D*, 79, 023512
- Zaharijas G., Hooper D., 2006, *Phys. Rev. D*, 73, 103501
- Zavala J., Vogelsberger M., Slatyer T. R., Loeb A., Springel V., 2011, *Phys. Rev. D*, 83, 123513
- Zhang L., Chen X., Kamionkowski M., Si Z.-G., Zheng Z., 2007, *Phys. Rev. D*, 76, 061301
- Zhang L., Chen X., Lei Y.-A., Si Z.-G., 2006, *Phys. Rev. D*, 74, 103519

APPENDIX A: OBSERVED INTENSITIES

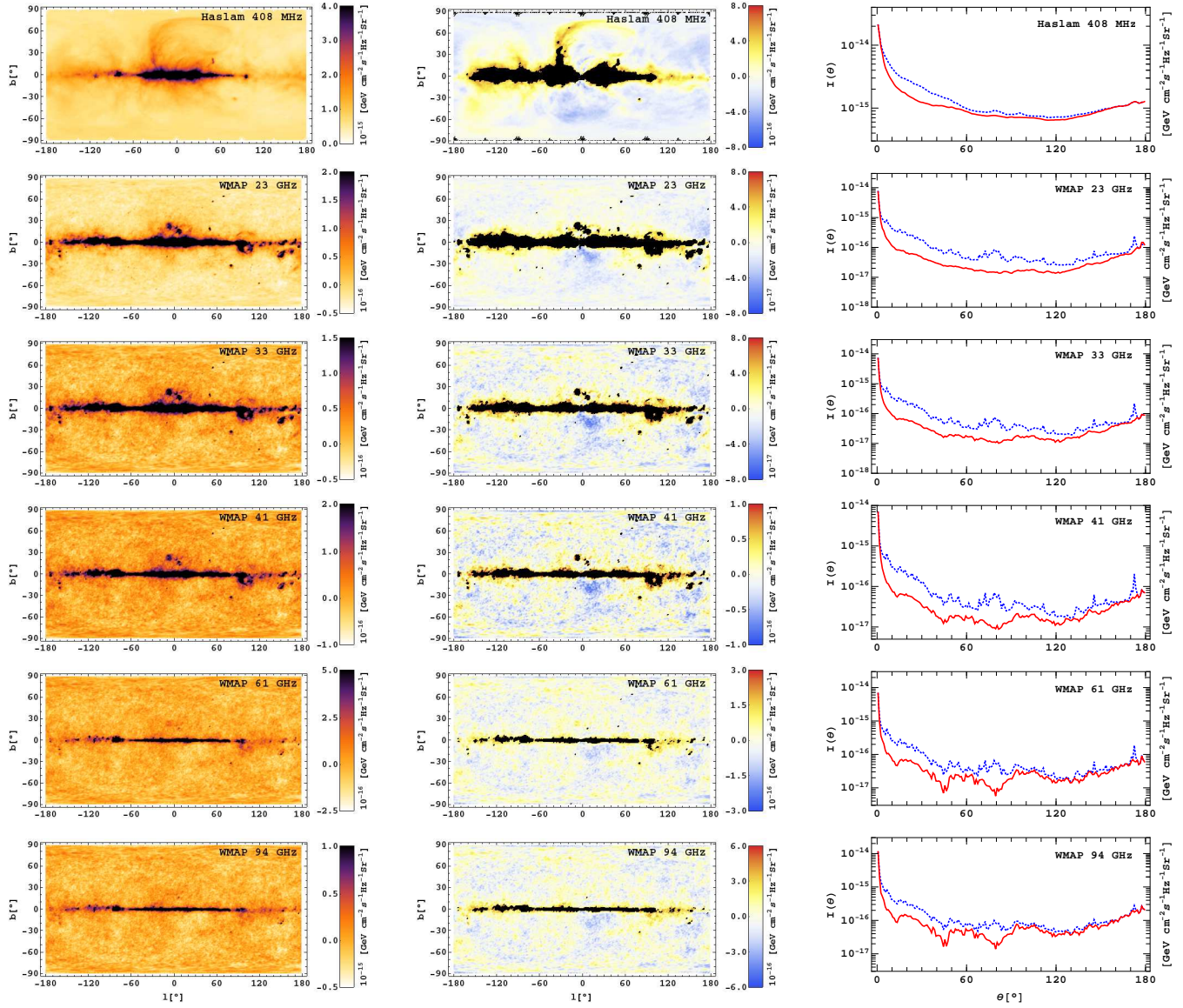


Figure A1. Haslam and WMAP intensity maps $I(l, b)$ in Galactic coordinates (left), masked residual maps $I(l, b) - I(\theta)$ (middle), and spherically-averaged intensities (right). Dotted blue lines represent the original mean intensity $I_0(\theta)$, while solid red lines correspond to the final intensity $I(\theta)$ after discarding the outliers (black areas in the masked residual maps).

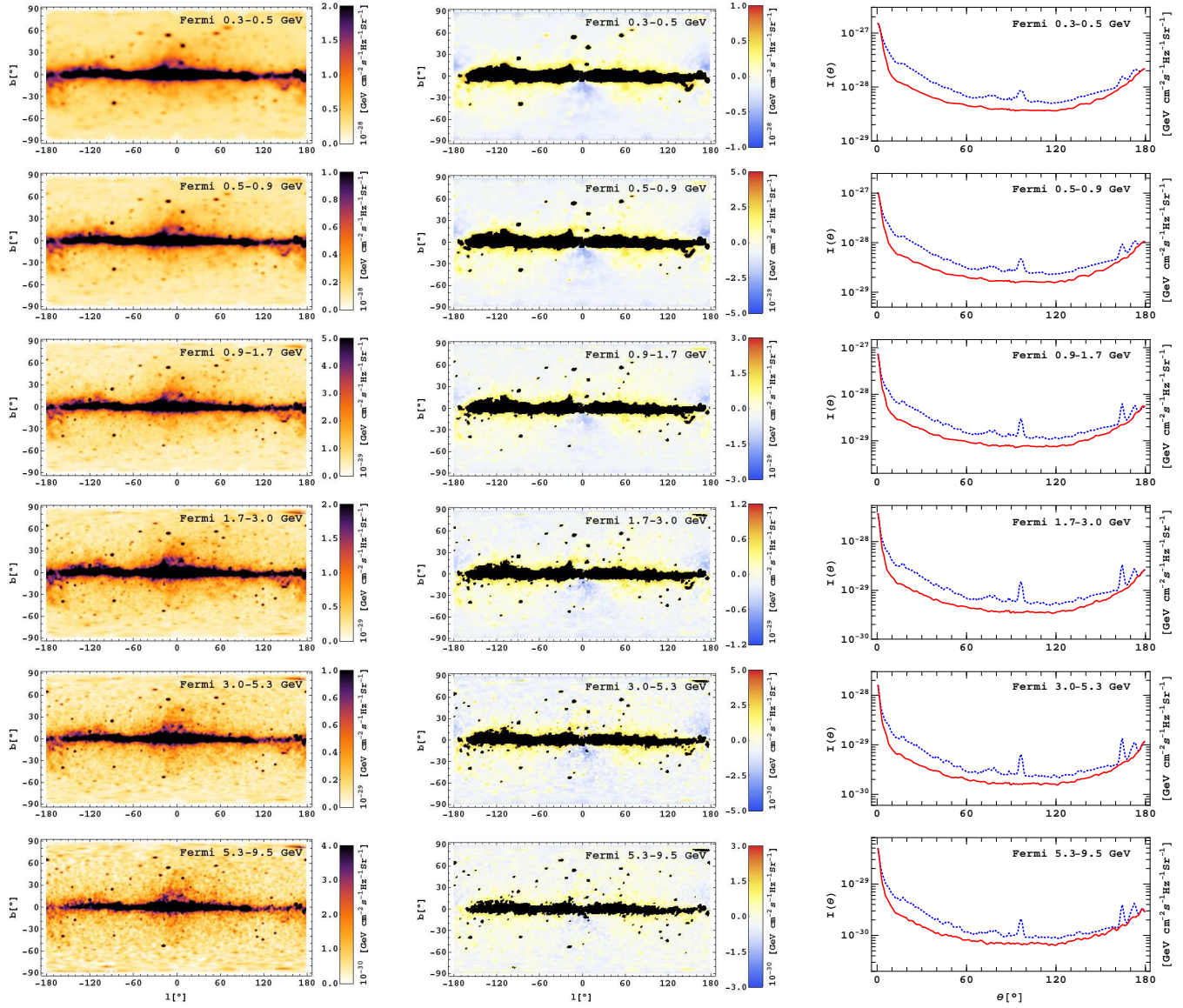


Figure A2. Fermi intensity maps $I(l, b)$ in Galactic coordinates (left), masked residual maps $I(l, b) - I(\theta)$ (middle), and spherically-averaged intensities (right). Dotted blue lines represent the original mean intensity $I_0(\theta)$, while solid red lines correspond to the final intensity $I(\theta)$ after discarding the outliers (black areas in the masked residual maps).

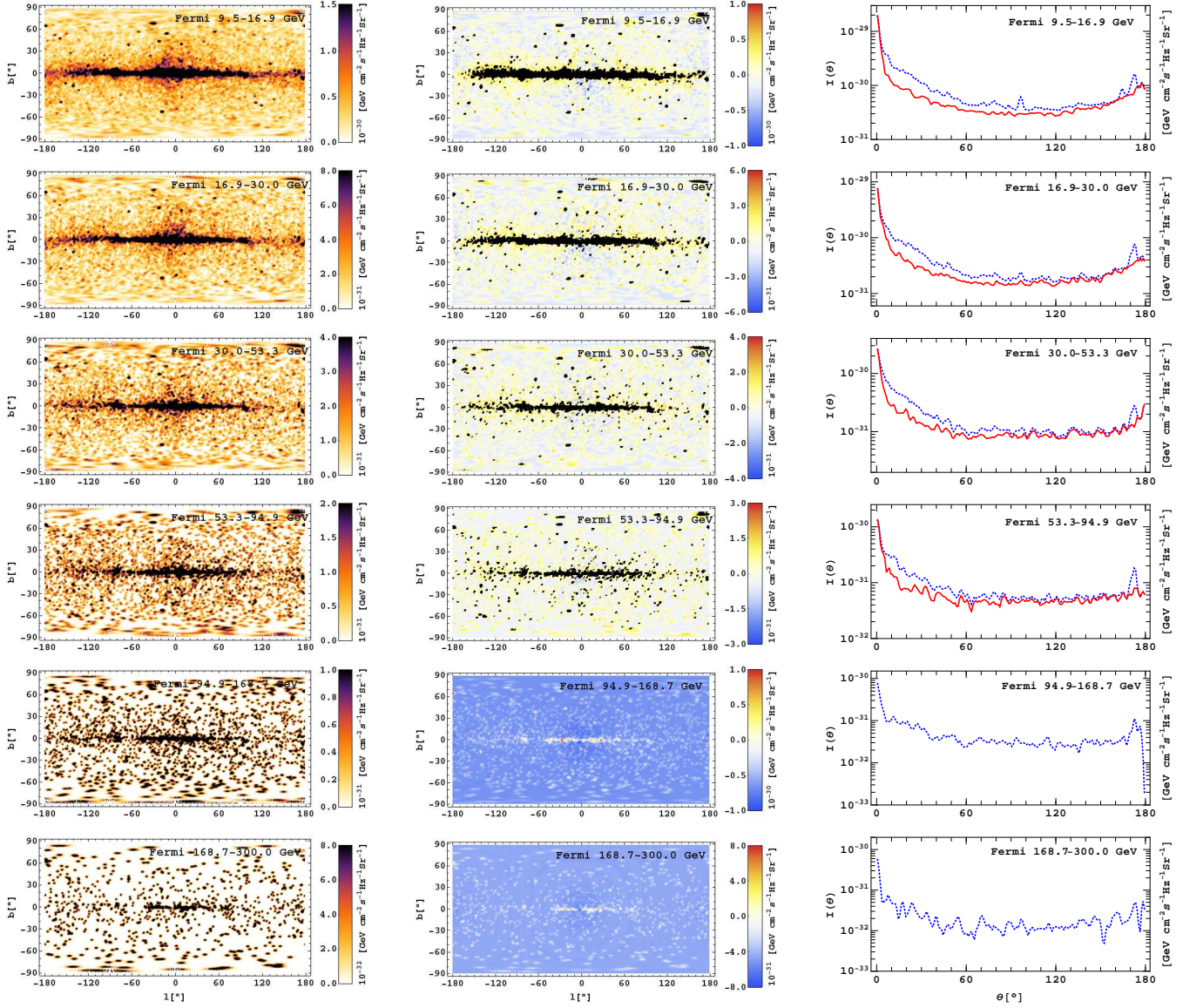


Figure A3. Fermi intensity maps $I(l, b)$ in Galactic coordinates (left), masked residual maps $I(l, b) - I(\theta)$ (middle), and spherically-averaged intensities (right). Dotted blue lines represent the original mean intensity $I_0(\theta)$, while solid red lines correspond to the final intensity $I(\theta)$ after discarding the outliers (black areas in the masked residual maps). For the last two bands, we opted to use the original average intensity $I_0(\theta)$ without applying any mask.

θ [°]	Haslam 408 MHz			23 GHz			33 GHz			WMAP			41 GHz			61 GHz		
	$I_0(\theta)$	$I(\theta)$ $\times 10^{-16}$	$\sigma(\theta)$	$I_0(\theta)$	$I(\theta)$ $\times 10^{-17}$	$\sigma(\theta)$	$I_0(\theta)$	$I(\theta)$ $\times 10^{-17}$	$\sigma(\theta)$	$I_0(\theta)$	$I(\theta)$ $\times 10^{-17}$	$\sigma(\theta)$	$I_0(\theta)$	$I(\theta)$ $\times 10^{-17}$	$\sigma(\theta)$	$I_0(\theta)$	$I(\theta)$ $\times 10^{-17}$	$\sigma(\theta)$
0.5	209.2	208.4	3.3	743.9	729.5	3.2	703.8	698.9	5.4	682.0	681.0	4.4	660.2	670.6	8.7			
1.5	147.7	145.6	3.5	210.4	202.3	3.7	167.8	148.8	4.0	147.8	119.0	5.8	137.3	98.8	11.7			
2.5	103.5	95.2	3.4	116.2	72.0	3.3	92.3	55.2	3.9	81.1	47.9	5.4	73.9	36.5	9.3			
3.5	84.8	73.9	3.6	90.6	43.8	2.9	72.5	33.0	3.8	64.0	27.9	5.0	58.9	26.6	9.6			
4.5	73.2	54.4	2.9	76.5	35.1	3.2	61.6	22.6	4.1	54.1	20.4	5.2	48.0	20.8	10.1			
5.5	64.9	44.1	2.5	67.6	24.2	3.3	54.0	17.9	3.5	47.0	15.3	4.3	40.3	13.2	8.6			
6.5	59.8	38.9	2.4	81.1	19.4	2.9	70.9	14.6	3.2	65.5	12.3	3.9	60.4	10.5	8.0			
7.5	53.4	34.4	2.7	63.2	17.1	2.9	52.1	12.6	2.8	46.4	11.5	4.0	41.1	10.7	7.8			
8.5	49.4	30.9	3.2	56.4	14.4	3.1	48.1	11.2	3.5	43.7	9.8	4.2	39.9	9.4	8.2			
9.5	44.4	28.3	2.9	43.6	12.1	3.1	34.8	9.6	3.5	30.1	8.4	4.1	25.2	8.0	8.3			
10.5	41.7	26.0	2.8	41.9	10.7	3.1	34.4	8.5	3.8	30.3	7.3	4.4	25.9	6.4	8.4			
12.5	36.3	22.1	2.7	34.2	8.6	2.9	27.9	6.7	3.3	24.5	6.0	4.2	21.0	4.7	7.5			
14.5	33.1	20.1	2.3	39.3	8.2	3.1	33.2	6.7	3.5	29.9	6.2	4.3	26.1	5.8	8.1			
16.5	30.3	18.2	2.3	32.0	7.7	3.1	26.4	6.5	3.5	23.5	6.5	4.4	21.4	7.1	8.2			
18.5	29.4	17.6	2.3	33.2	7.3	3.2	28.2	6.2	3.5	25.5	6.0	4.4	23.7	6.8	8.5			
20.5	27.7	15.9	2.2	24.5	6.5	3.2	19.7	6.0	3.9	17.2	5.9	4.9	15.3	6.2	9.1			
25.5	23.6	13.6	1.9	19.9	5.8	3.0	16.1	4.8	3.3	14.2	4.7	4.4	12.8	5.2	8.3			
30.5	21.3	12.3	2.1	17.8	4.4	2.1	14.7	3.5	2.8	13.1	3.2	3.7	12.0	3.2	7.6			
40.5	16.1	11.0	2.5	8.5	2.9	1.7	6.4	2.1	2.3	5.5	1.8	3.2	4.6	1.6	7.1			
50.5	13.0	10.3	2.5	6.7	2.3	1.4	5.3	1.8	2.0	4.6	1.7	2.9	4.5	1.9	6.7			
60.5	9.7	8.7	2.2	4.2	2.0	1.6	3.4	1.7	2.3	3.1	1.7	3.2	3.3	2.1	7.1			
70.5	8.7	7.6	1.6	4.7	1.7	1.3	4.0	1.5	2.1	3.8	1.5	3.1	3.9	1.8	6.8			
80.5	9.0	7.5	1.7	6.8	1.5	1.4	5.8	1.2	2.0	5.3	1.1	3.0	4.9	1.0	6.6			
90.5	8.0	7.2	1.9	4.1	1.4	1.3	3.4	1.3	2.2	3.0	1.4	3.3	3.0	1.8	7.0			
100.5	7.6	7.0	1.7	3.5	1.8	1.6	3.0	1.8	2.3	3.0	1.9	3.1	3.5	2.8	6.9			
110.5	7.5	6.7	1.7	3.7	1.5	1.6	3.1	1.4	2.5	2.9	1.6	3.6	3.2	2.3	7.5			
120.5	7.2	6.5	1.8	2.6	1.4	1.5	2.0	1.2	2.4	1.8	1.2	3.4	1.8	1.4	7.4			
130.5	7.5	6.9	2.1	2.6	1.8	1.8	2.0	1.5	2.7	1.7	1.4	3.7	1.6	1.4	7.7			
140.5	8.3	7.7	2.3	4.1	2.8	2.2	3.1	2.2	2.7	2.7	2.0	3.7	2.7	2.2	8.1			
150.5	9.4	9.0	2.0	5.3	3.0	2.1	4.1	2.4	2.8	3.6	2.5	4.0	3.5	2.7	8.2			
155.5	9.9	9.8	2.2	5.5	3.8	2.4	4.1	3.2	2.9	3.6	2.8	3.8	3.4	3.0	8.0			
160.5	10.6	10.5	1.7	6.1	4.8	2.5	4.8	4.0	2.7	4.2	3.9	3.6	4.2	4.1	7.3			
162.5	10.7	10.7	1.6	6.1	5.3	2.5	4.6	4.3	2.7	4.0	3.9	3.4	4.1	4.1	7.1			
164.5	10.7	10.7	1.5	6.2	5.6	2.6	4.7	4.6	2.8	4.1	4.1	3.4	4.5	4.5	7.3			
166.5	10.9	10.9	1.6	6.8	6.0	2.8	5.3	4.8	2.8	4.7	4.4	3.5	5.3	5.2	7.4			
168.5	11.2	11.2	1.7	7.1	5.9	2.3	5.2	4.8	2.9	4.4	4.2	3.6	4.6	4.5	7.4			
170.5	12.1	12.1	1.8	10.6	6.2	1.9	8.5	4.9	2.9	7.7	4.9	4.1	8.1	6.2	8.5			
171.5	12.4	12.4	1.8	10.5	7.0	2.3	8.0	5.7	3.0	7.1	5.4	4.1	7.5	7.0	8.5			
172.5	12.7	12.7	2.0	24.3	7.8	2.2	21.5	5.8	2.3	19.9	5.1	3.5	18.6	6.2	7.9			
173.5	12.6	12.6	1.9	14.5	9.0	2.4	10.8	6.6	2.5	9.1	5.5	3.3	8.2	6.0	7.6			
174.5	12.3	12.3	1.9	10.4	9.9	2.7	7.6	7.4	2.6	6.4	6.3	3.2	6.7	6.7	6.7			
175.5	12.0	12.0	1.6	9.3	9.2	2.5	6.6	6.6	2.5	5.3	5.3	3.0	4.9	4.9	6.4			
176.5	12.0	12.0	1.4	10.1	9.8	3.0	7.1	7.1	2.8	5.8	5.8	3.0	5.4	5.4	5.9			
177.5	12.4	12.4	1.3	12.5	14.7	2.3	9.7	9.3	3.8	8.3	8.2	4.1	9.0	9.0	7.7			
178.5	12.4	12.4	1.2	12.4	14.7	2.5	8.9	8.9	3.5	7.4	7.4	3.5	6.9	6.9	6.2			
179.5	12.7	12.7	0.9	12.4	12.4	2.9	8.9	8.9	2.7	7.0	7.0	2.6	6.0	6.0	4.9			

Table A1. Haslam and WMAP: Original observational mean intensity $I_0(\theta)$, final mean intensity after discarding the outliers $I(\theta)$, and standard deviation $\sigma(\theta)$, in units of $\text{GeV cm}^{-2} \text{s}^{-1} \text{Hz}^{-1} \text{sr}^{-1}$.

θ [°]	WMAP 94 GHz			0.3-0.5 GeV			0.5-0.9 GeV			Fermi 0.9-1.7 GeV			1.7-3.0 GeV		
	$I_0(\theta)$	$I(\theta)$ $\times 10^{-17}$	$\sigma(\theta)$	$I_0(\theta)$	$I(\theta)$ $\times 10^{-30}$	$\sigma(\theta)$	$I_0(\theta)$	$I(\theta)$ $\times 10^{-30}$	$\sigma(\theta)$	$I_0(\theta)$	$I(\theta)$ $\times 10^{-30}$	$\sigma(\theta)$	$I_0(\theta)$	$I(\theta)$ $\times 10^{-30}$	$\sigma(\theta)$
0.5	1097.8	1132.3	22.2	1500.2	1506.8	34.3	989.9	1016.7	18.7	713.6	725.8	9.1	367.7	371.1	4.6
1.5	287.4	219.6	24.5	1295.6	1353.7	37.3	774.3	790.1	16.6	447.3	462.2	9.8	230.1	245.2	4.7
2.5	140.3	66.9	21.4	1037.0	992.3	37.0	553.9	508.8	19.8	275.9	219.7	9.9	139.7	116.5	4.9
3.5	114.6	52.3	21.2	826.8	689.0	34.2	418.4	304.9	16.7	211.3	129.4	8.8	106.7	66.6	4.0
4.5	85.1	39.9	21.8	680.6	460.1	36.1	340.2	208.4	17.8	174.1	107.2	9.1	86.8	53.3	4.3
5.5	69.9	25.3	19.2	585.4	358.1	34.3	293.0	170.4	16.8	146.5	82.5	8.3	71.8	36.7	4.4
6.5	86.1	20.6	18.3	509.1	289.2	32.1	258.2	133.7	16.1	129.9	56.2	9.3	63.4	26.9	4.1
7.5	66.6	20.8	17.8	470.1	213.9	38.6	243.3	101.3	19.3	126.2	47.8	7.7	61.7	23.8	3.9
8.5	61.9	18.0	18.1	415.0	184.3	35.3	211.3	90.0	17.5	107.7	42.6	8.0	52.1	21.5	3.8
9.5	43.2	15.7	18.6	367.1	165.0	33.0	181.9	80.7	16.7	89.5	38.4	8.1	42.9	19.5	3.6
10.5	41.6	12.5	19.0	341.4	150.7	31.9	167.5	74.2	17.0	83.5	36.8	8.6	39.8	18.3	3.9
12.5	33.5	9.1	17.5	285.3	132.9	30.0	137.5	61.5	14.8	67.8	30.3	7.7	32.2	14.8	3.5
14.5	39.5	11.7	18.5	271.2	123.1	31.7	130.1	56.9	15.8	63.7	28.2	8.0	31.5	13.5	3.5
16.5	36.6	14.3	18.5	272.5	117.7	35.1	135.2	55.0	16.8	70.1	27.2	8.3	34.5	13.2	3.9
18.5	39.0	15.0	19.4	264.6	110.3	34.7	132.4	51.7	16.7	66.6	25.7	8.7	32.2	12.3	4.0
20.5	27.8	13.2	20.5	241.1	106.6	33.4	118.3	49.9	16.6	57.9	23.7	8.1	28.0	11.5	4.0
25.5	22.9	11.1	18.4	193.1	89.0	27.0	93.5	40.1	12.4	46.3	19.7	6.7	22.7	9.6	3.2
30.5	20.9	7.0	17.4	160.3	76.2	21.4	78.9	36.0	11.1	39.1	17.7	6.1	18.6	8.3	2.7
40.5	9.3	3.5	15.9	115.6	60.7	19.6	56.0	27.9	10.0	27.8	13.2	5.1	13.4	6.4	2.4
50.5	9.4	4.4	15.2	87.4	50.2	16.8	41.5	22.6	8.3	19.8	10.6	4.5	9.7	5.2	2.2
60.5	7.3	4.9	16.1	65.4	45.1	18.4	30.1	20.0	9.3	14.4	9.5	4.8	6.8	4.5	2.3
70.5	7.3	4.0	15.1	63.3	43.4	16.7	29.2	19.1	8.4	13.6	8.7	4.3	6.5	4.1	2.0
80.5	7.7	2.2	14.9	63.3	39.2	16.0	29.2	17.1	7.7	14.0	8.0	3.9	6.5	3.7	1.8
90.5	6.4	3.9	15.6	59.4	37.4	15.7	27.4	16.3	8.2	13.0	7.8	4.6	6.0	3.6	2.1
100.5	7.7	6.2	15.4	57.8	37.4	15.6	25.9	16.6	7.9	12.0	7.9	4.3	5.7	3.8	2.1
110.5	6.9	5.1	16.6	54.1	36.8	15.0	25.2	15.9	7.6	11.9	7.4	4.0	5.6	3.5	2.0
120.5	4.5	3.5	16.6	51.3	36.3	13.8	23.7	16.0	7.0	11.4	7.4	3.5	5.5	3.6	1.9
130.5	4.1	3.7	17.6	57.2	40.2	15.6	26.1	17.5	7.7	12.3	8.2	3.8	5.8	3.8	1.8
140.5	6.8	5.6	18.9	70.5	49.4	20.4	32.8	21.4	9.6	15.7	10.2	4.9	7.1	4.9	2.4
150.5	8.6	7.0	19.0	83.2	60.0	26.1	39.3	27.2	12.5	19.1	13.4	6.6	8.7	6.1	2.9
155.5	8.3	7.9	18.8	89.8	71.3	29.5	42.7	31.9	14.1	20.3	14.7	6.9	9.2	6.9	3.3
160.5	10.3	10.1	16.9	100.4	84.8	31.2	46.4	39.5	15.4	21.6	18.6	7.7	9.8	8.5	3.4
162.5	10.9	10.8	16.8	126.4	94.1	36.9	63.9	41.8	16.9	29.0	20.8	8.9	13.7	9.2	3.9
164.5	12.3	12.3	16.8	156.4	102.5	38.7	92.6	47.2	19.3	62.2	22.1	9.2	33.5	9.8	3.9
166.5	14.6	14.4	17.3	142.8	109.6	36.7	68.4	49.1	18.0	29.7	23.2	9.1	13.9	10.8	4.1
168.5	13.5	13.3	17.3	141.5	121.4	34.7	65.7	51.8	14.7	30.2	25.2	7.7	13.7	11.4	3.7
170.5	20.0	17.8	19.9	173.4	129.9	33.0	83.6	60.1	16.0	41.2	28.7	7.9	19.3	13.5	3.7
171.5	19.7	19.7	19.5	194.1	138.3	31.3	96.7	62.7	14.3	47.6	30.7	7.5	22.6	14.1	3.6
172.5	27.8	17.7	18.1	209.0	154.7	33.0	107.2	68.0	13.2	57.2	35.8	8.2	27.6	15.2	3.4
173.5	20.9	19.0	17.5	212.6	164.2	29.3	106.9	79.6	16.3	55.3	39.7	7.8	26.1	17.3	3.9
174.5	20.4	20.5	15.7	203.9	172.7	26.6	95.7	82.0	13.2	44.9	41.2	7.6	20.5	19.0	3.7
175.5	16.4	16.4	14.7	196.7	179.6	25.3	90.4	85.5	12.7	42.5	42.3	7.6	19.4	19.4	3.6
176.5	18.1	18.1	13.9	196.4	193.0	29.5	92.9	92.9	14.6	45.1	45.5	8.7	20.7	20.5	4.1
177.5	26.8	26.6	18.5	203.1	203.1	26.9	98.7	98.7	14.9	49.5	53.3	9.2	23.0	23.1	4.5
178.5	22.4	22.4	14.9	211.8	211.8	21.3	103.2	103.2	13.2	52.3	55.7	9.3	24.9	24.9	4.0
179.5	21.0	21.0	13.2	217.6	217.6	10.8	105.3	105.3	7.0	54.5	54.5	6.4	26.2	26.2	2.1

Table A2. WMAP and Fermi: Original observational mean intensity $I_0(\theta)$, final mean intensity after discarding the outliers $I(\theta)$, and standard deviation $\sigma(\theta)$, in units of $\text{GeV cm}^{-2} \text{ s}^{-1} \text{ Hz}^{-1} \text{ sr}^{-1}$.

θ [°]	Fermi											
	3.0-5.3 GeV			5.3-9.5 GeV			9.5-16.9 GeV			16.9-30.0 GeV		
	$I_0(\theta)$	$I(\theta)$ $\times 10^{-31}$	$\sigma(\theta)$	$I_0(\theta)$	$I(\theta)$ $\times 10^{-31}$	$\sigma(\theta)$	$I_0(\theta)$	$I(\theta)$ $\times 10^{-31}$	$\sigma(\theta)$	$I_0(\theta)$	$I(\theta)$ $\times 10^{-31}$	$\sigma(\theta)$
0.5	1554.0	1574.6	19.2	482.4	488.9	7.5	188.8	195.6	3.1	74.4	75.7	1.8
1.5	950.3	941.4	17.8	311.6	321.6	7.5	118.7	116.7	3.4	45.9	44.7	2.2
2.5	577.1	468.4	20.9	201.6	163.2	7.3	71.7	60.3	3.7	29.3	23.3	1.9
3.5	443.4	278.5	17.8	158.6	101.2	7.1	51.5	37.5	3.4	23.3	19.1	1.7
4.5	360.0	220.5	18.4	129.0	82.1	7.9	42.7	27.8	3.6	19.3	16.0	2.0
5.5	305.0	181.7	17.6	106.7	60.1	7.3	38.6	16.9	3.2	17.3	11.9	1.9
6.5	274.4	149.0	15.7	93.0	53.1	6.1	36.6	15.6	3.4	15.6	9.4	2.1
7.5	263.3	109.0	21.7	89.9	47.3	6.7	36.2	15.5	3.3	14.9	9.1	2.0
8.5	221.0	94.7	17.7	78.7	41.4	8.0	30.5	13.9	3.4	13.4	7.2	2.2
9.5	182.7	85.8	15.3	67.2	36.6	8.2	24.7	11.9	3.1	11.3	6.1	1.9
10.5	169.4	78.0	17.2	63.0	33.2	7.8	22.4	11.2	3.2	10.4	5.7	1.8
12.5	140.5	66.4	16.2	52.6	27.1	6.7	20.3	10.0	3.2	8.8	4.8	1.8
14.5	132.9	65.9	16.5	49.9	25.6	6.6	19.5	9.5	3.1	9.1	5.4	1.9
16.5	146.3	61.7	16.4	52.4	24.0	7.1	18.9	8.6	2.5	8.8	4.6	1.7
18.5	136.3	53.9	16.5	50.5	22.6	6.6	18.0	8.5	2.8	7.5	3.9	1.7
20.5	116.8	51.4	17.0	44.6	20.4	5.9	17.0	8.5	3.0	7.9	4.0	1.7
25.5	94.5	42.6	15.2	35.2	17.1	5.3	12.9	6.0	2.5	6.0	2.8	1.5
30.5	79.0	36.8	10.6	29.7	14.5	5.0	10.9	6.3	2.2	5.2	3.0	1.4
40.5	57.8	29.6	10.6	21.2	11.2	4.7	8.1	4.8	2.2	3.6	2.2	1.1
50.5	39.8	21.8	8.7	15.7	9.5	4.3	5.9	4.1	2.0	2.7	1.9	1.2
60.5	28.3	19.9	9.5	11.6	8.2	3.6	4.5	3.3	1.7	2.1	1.6	1.1
70.5	27.0	18.1	9.0	11.1	7.8	4.1	4.6	3.3	1.9	2.1	1.5	1.1
80.5	27.7	16.5	7.5	11.3	7.2	3.8	4.5	3.0	1.7	2.2	1.7	1.2
90.5	25.7	16.0	8.6	9.7	6.9	3.5	3.8	2.9	1.8	1.8	1.5	1.0
100.5	23.6	16.2	8.6	9.2	6.7	4.0	3.6	3.0	1.9	1.7	1.4	1.1
110.5	23.8	15.7	8.4	9.3	6.9	3.7	3.9	3.0	1.9	2.1	1.7	1.2
120.5	22.6	15.4	7.9	8.8	6.5	3.4	3.5	2.7	1.7	1.7	1.5	1.0
130.5	24.3	17.8	9.2	9.9	7.8	4.3	4.0	3.0	1.9	1.9	1.8	1.2
140.5	30.0	21.3	11.2	10.9	8.6	4.5	4.4	3.7	2.1	2.0	1.7	1.2
150.5	35.2	26.1	12.5	12.9	10.7	5.3	4.6	3.8	2.1	1.9	1.7	1.2
155.5	38.6	29.0	14.1	13.9	12.0	5.8	4.7	4.4	2.2	2.3	2.3	1.3
160.5	39.4	35.3	15.1	13.6	12.5	4.7	5.4	5.3	2.4	2.7	2.6	1.5
162.5	54.9	39.4	18.1	17.6	14.2	6.0	6.2	5.8	2.4	2.7	2.4	1.4
164.5	134.4	42.9	17.0	39.3	16.1	5.8	8.8	5.6	2.7	2.9	2.4	1.5
166.5	55.7	46.1	18.1	18.6	15.5	5.1	6.9	6.3	2.3	2.9	2.8	1.6
168.5	54.8	46.9	16.9	19.9	17.6	5.6	7.0	6.6	2.5	3.3	3.0	1.6
170.5	82.7	53.7	14.5	30.4	21.6	6.2	11.2	6.8	2.7	5.3	3.2	1.4
171.5	94.7	54.1	14.7	35.3	22.6	6.2	13.0	6.7	2.7	5.9	3.3	1.5
172.5	111.4	58.4	17.4	41.5	22.9	6.1	16.2	7.4	2.9	7.7	3.6	1.6
173.5	103.5	65.2	15.4	37.0	22.5	5.9	15.0	8.7	2.8	7.2	3.7	1.8
174.5	79.0	69.2	11.6	27.6	24.0	6.5	10.2	9.4	2.1	4.6	3.9	1.8
175.5	75.4	74.7	14.8	26.1	24.8	5.6	9.2	9.0	2.2	3.9	3.9	1.3
176.5	81.8	81.8	17.2	28.4	28.3	6.1	9.9	9.2	2.4	4.3	4.3	1.5
177.5	93.7	98.6	18.4	32.7	31.9	7.2	11.2	11.0	2.4	4.8	3.9	1.4
178.5	105.6	109.0	22.0	32.5	32.4	7.1	10.3	10.3	1.5	4.6	4.2	1.7
179.5	116.3	116.3	14.9	29.1	29.1	3.6	8.6	8.6	0.5	3.8	3.8	0.8

Table A3. Fermi: Original observational mean intensity $I_0(\theta)$, final mean intensity after discarding the outliers $I(\theta)$, and standard deviation $\sigma(\theta)$, in units of $\text{GeV cm}^{-2} \text{s}^{-1} \text{Hz}^{-1} \text{sr}^{-1}$.

θ [°]	Fermi							
	30.0-53.3 GeV			53.3-94.9 GeV			94.9-168.7 GeV	168.7-300.0 GeV
	$I_0(\theta)$	$I(\theta)$ $\times 10^{-32}$	$\sigma(\theta)$	$I_0(\theta)$	$I(\theta)$ $\times 10^{-32}$	$\sigma(\theta)$	$I_0(\theta)$ $\times 10^{-32}$	$I_0(\theta)$ $\times 10^{-32}$
0.5	253.5	263.1	13.8	130.5	134.0	8.7	75.5	56.9
1.5	189.2	183.6	14.5	96.3	101.4	9.4	50.7	31.4
2.5	144.4	113.8	12.9	63.8	50.9	8.6	32.1	13.4
3.5	115.9	76.8	12.3	44.4	37.2	9.4	22.3	5.4
4.5	97.8	58.0	13.2	37.4	33.1	8.4	17.5	4.8
5.5	86.2	47.6	11.4	34.1	27.0	7.5	12.4	5.6
6.5	71.5	39.8	9.9	32.1	15.3	9.3	9.6	5.7
7.5	71.0	32.1	12.8	32.5	17.3	9.1	10.0	7.5
8.5	64.3	29.7	12.5	30.1	18.1	9.3	9.5	6.6
9.5	55.4	27.6	11.1	28.2	14.3	8.6	9.6	5.2
10.5	55.1	28.4	11.9	29.8	14.0	9.0	11.9	4.7
12.5	48.5	25.3	11.8	27.8	12.6	8.4	10.7	4.6
14.5	44.0	20.9	11.4	20.1	10.1	6.9	8.8	1.9
16.5	43.7	21.0	10.2	17.2	7.3	6.0	8.2	4.2
18.5	39.7	21.9	11.1	17.9	8.0	7.0	9.1	3.7
20.5	39.2	22.7	11.4	13.4	7.8	6.1	9.5	2.5
25.5	28.9	16.5	9.8	14.4	9.1	6.6	7.1	3.5
30.5	21.8	13.7	9.4	10.9	6.3	6.0	6.3	2.0
40.5	19.1	13.4	8.6	8.5	6.6	6.2	4.2	2.0
50.5	11.1	8.0	6.7	6.8	4.4	5.0	4.6	1.1
60.5	9.4	7.7	6.9	6.2	5.0	5.5	2.4	0.8
70.5	11.4	8.9	8.2	5.9	4.8	5.1	3.6	2.3
80.5	11.6	8.6	7.2	5.9	4.1	5.1	2.8	1.1
90.5	8.9	7.9	7.7	5.5	4.8	5.5	2.4	1.5
100.5	8.3	7.5	6.5	5.2	4.8	5.4	2.7	0.9
110.5	9.4	8.3	7.9	5.1	4.0	5.2	2.7	1.1
120.5	8.3	7.7	7.0	5.6	5.3	5.4	2.6	1.2
130.5	11.5	10.6	8.5	5.0	4.5	5.4	2.4	1.4
140.5	9.6	8.7	8.0	6.0	4.9	5.4	3.5	1.5
150.5	10.9	9.3	7.9	6.4	5.2	5.4	2.8	1.1
155.5	9.6	8.4	7.5	5.3	5.1	5.4	3.3	1.2
160.5	11.3	10.6	8.3	5.7	5.2	5.7	3.1	2.7
162.5	9.8	9.0	7.6	6.0	5.0	5.9	3.4	2.6
164.5	12.4	11.6	9.1	6.9	6.3	6.0	3.8	1.5
166.5	12.8	11.6	7.5	5.6	5.5	5.5	3.4	1.7
168.5	11.6	11.5	8.7	6.6	5.9	5.8	3.5	1.8
170.5	20.9	13.3	9.5	12.1	5.9	5.2	5.3	2.6
171.5	23.4	12.9	9.4	13.7	6.3	5.1	6.9	3.4
172.5	27.9	12.0	9.1	18.2	8.0	6.3	11.0	4.7
173.5	26.4	14.0	8.5	16.7	7.9	6.8	9.6	4.9
174.5	19.3	17.7	9.7	9.4	8.0	6.7	5.5	3.3
175.5	17.6	16.8	9.6	6.3	6.3	5.5	6.5	1.3
176.5	16.3	16.3	9.5	5.6	5.6	5.3	7.3	0.9
177.5	17.8	17.8	9.1	6.4	6.4	5.8	4.6	3.5
178.5	25.0	25.0	10.3	6.9	6.9	6.0	1.3	5.2
179.5	29.7	29.7	9.3	6.3	6.3	4.0	0.2	3.4

Table A4. Fermi: Original observational mean intensity $I_0(\theta)$, final mean intensity after discarding the outliers $I(\theta)$, and standard deviation $\sigma(\theta)$, in units of $\text{GeV cm}^{-2} \text{ s}^{-1} \text{ Hz}^{-1} \text{ sr}^{-1}$.